Immunity

trans-Endothelial neutrophil migration activates bactericidal function via Piezo1 mechanosensing

Graphical abstract

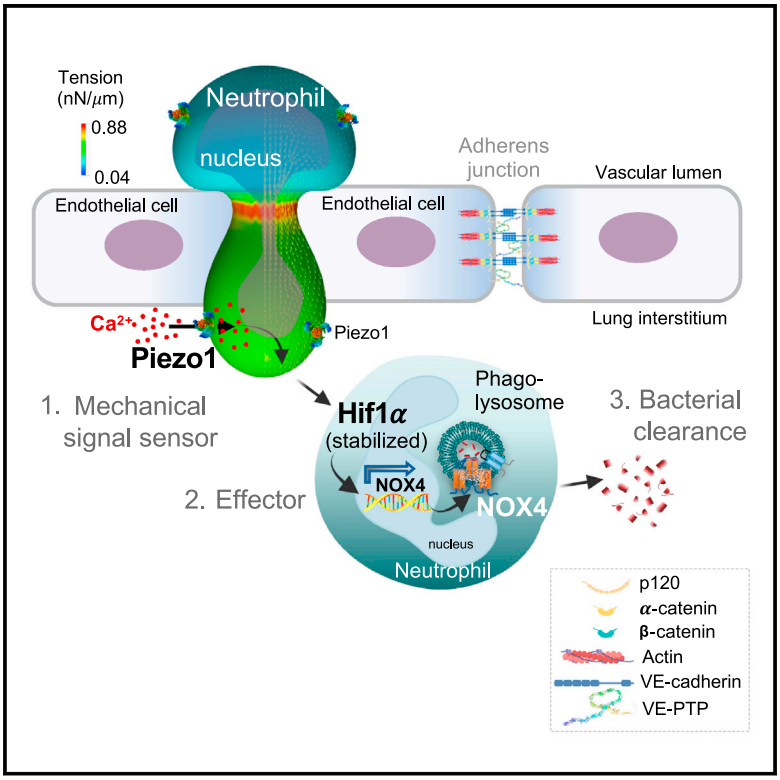

Highlights

- *trans*-Endothelial migration regulates transcription and antimicrobial function of PMNs
- Increased membrane tension during transmigration triggers Piezo1 gating and Ca^{2+} influx
- Piezo1 signals transcriptional upregulation of *Nox4* via Hif1α stabilization

Authors

Amitabha Mukhopadhyay, Yoshikazu Tsukasaki, Wan Ching Chan, ..., Balaji Ganesh, Yulia Komarova, Asrar B. Malik

Correspondence

ykomarov@uic.edu (Y.K.), abmalik@uic.edu (A.B.M.)

In brief

PMN migration through restrictive endothelial junction generates mechanical tension on the PMN plasma membrane, but its impact on PMN function or immune response is unknown. Mukhopadhyay et. al. showed that Piezo1-mediated mechanosensing during transmigration enhanced bacterial killing function of PMNs in tissue via NOX4 and prevented inflammatory tissue injury.

Mukhopadhyay et al., 2024, Immunity *57*, 1–16
January 9, 2024
https://doi.org/10.1016/j.immuni.2023.11.007

CellPress

Immunity

CellPress
OPEN ACCESS

Article

trans-Endothelial neutrophil migration activates bactericidal function via Piezo1 mechanosensing

Amitabha Mukhopadhyay,[1] Yoshikazu Tsukasaki,[1] Wan Ching Chan,[1] Jonathan P. Le,[1] Man Long Kwok,[1] Jian Zhou,[2] Viswanathan Natarajan,[1,3] Nima Mostafazadeh,[2] Mark Maienschein-Cline,[4] Ian Papautsky,[2] Chinnaswamy Tiruppathi,[1] Zhangli Peng,[2] Jalees Rehman,[1] Balaji Ganesh,[5] Yulia Komarova,[1,*] and Asrar B. Malik[1,6,*]

[1]Department of Pharmacology and Regenerative Medicine and The Center for Lung and Vascular Biology, University of Illinois College of Medicine, Chicago, IL 60612, USA
[2]Richard and Loan Hill Department of Biomedical Engineering, University of Illinois, Chicago, IL 60612, USA
[3]Department of Medicine, University of Illinois College of Medicine, Chicago, IL 60612, USA
[4]Research Informatics Core, Research Resources Center, University of Illinois College of Medicine, Chicago, IL 60612, USA
[5]Flow Cytometry Core, Research Resources Center, University of Illinois College of Medicine, Chicago, IL 60612, USA
[6]Lead contact
*Correspondence: ykomarov@uic.edu (Y.K.), abmalik@uic.edu (A.B.M.)
https://doi.org/10.1016/j.immuni.2023.11.007

SUMMARY

The regulation of polymorphonuclear leukocyte (PMN) function by mechanical forces encountered during their migration across restrictive endothelial cell junctions is not well understood. Using genetic, imaging, microfluidic, and *in vivo* approaches, we demonstrated that the mechanosensor Piezo1 in PMN plasmalemma induced spike-like Ca^{2+} signals during *trans*-endothelial migration. Mechanosensing increased the bactericidal function of PMN entering tissue. Mice in which Piezo1 in PMNs was genetically deleted were defective in clearing bacteria, and their lungs were predisposed to severe infection. Adoptive transfer of Piezo1-activated PMNs into the lungs of *Pseudomonas aeruginosa*-infected mice or exposing PMNs to defined mechanical forces in microfluidic systems improved bacterial clearance phenotype of PMNs. Piezo1 transduced the mechanical signals activated during transmigration to upregulate nicotinamide adenine dinucleotide phosphate (NADPH) oxidase 4, crucial for the increased PMN bactericidal activity. Thus, Piezo1 mechanosensing of increased PMN tension, while traversing the narrow endothelial adherens junctions, is a central mechanism activating the host-defense function of transmigrating PMNs.

INTRODUCTION

Polymorphonuclear leukocytes (PMNs) generate reactive oxygen species (ROS) and serve as the first line of defense against pathogens such as bacteria and fungi.[1,2] PMNs are particularly important for the lung's defense function in response to air borne irritants and pathogens.[3–5] Circulating PMNs receiving chemoattractant signals from infected tissue are mobilized in the lung interstitium and airspace upon transmigrating through the restrictive endothelial adherens junctions (AJs) and alveolar epithelial barrier[6,7]. Due to the large PMN diameter ranging from 8.7 to 13 μm in humans[8–11] relative to the narrow slit-like pores of AJs (mean diameter of 4 nm in most continuous endothelial barriers),[7,12] the PMN plasma membrane breaching the AJs experiences unusually high tension and stretching during the transmigration event.[13] We surmised that physical constraints at the junctions may influence PMN transmigration and functional properties such as their fitness for host defense and bacterial killing.[14]

The *trans*-endothelial junctional route is responsible for approximately 90% of PMN migration across continuous endothelial barriers.[15,16] An essential host-defense function of PMNs is to activate the phagocytic machinery and kill bacterial pathogens through proteases and ROS production.[17] Phagocytosis is a multifaceted process consisting of pathogen recognition, engulfment, and elimination.[18,19] Bacterial killing is driven largely by nicotinamide adenine dinucleotide phosphate (NADPH) oxidases[20] and maturation of phagosomes into phagolysosomes, the organelles with oxidative and lytic properties.[18,19] PMNs express several NADPH oxidase isoforms, NOX1, NOX2, and NOX4, using NADPH to generate ROS.[20] The function of redox signaling in the mechanism of PMN innate immune function via NOX2 was described in patients with chronic granulomatous disease[21,22,23] who are highly susceptible to bacterial and fungal infections.[24,25,26] While the canonical mechanism of Nox2 activation in PMN bactericidal function is understood,[27] less is known about other NOX isoforms in the PMN anti-bactericidal function.

Here, we used multiple approaches to investigate the role of mechanical signals generated during PMN migration across the restrictive endothelial junction barrier in activating the PMN host-defense function. We demonstrated that mechanical forces acting on PMNs sensed by Piezo1[28,29] during transmigration induced the expression of Nox4, a constitutively active NADPH oxidase producing hydrogen peroxide.[30,31,32] In contrast, Nox2 was not altered. These findings show the immune regulatory

Please cite this article in press as: Mukhopadhyay et al., *trans*-Endothelial neutrophil migration activates bactericidal function via Piezo1 mechanosensing, Immunity (2023), https://doi.org/10.1016/j.immuni.2023.11.007

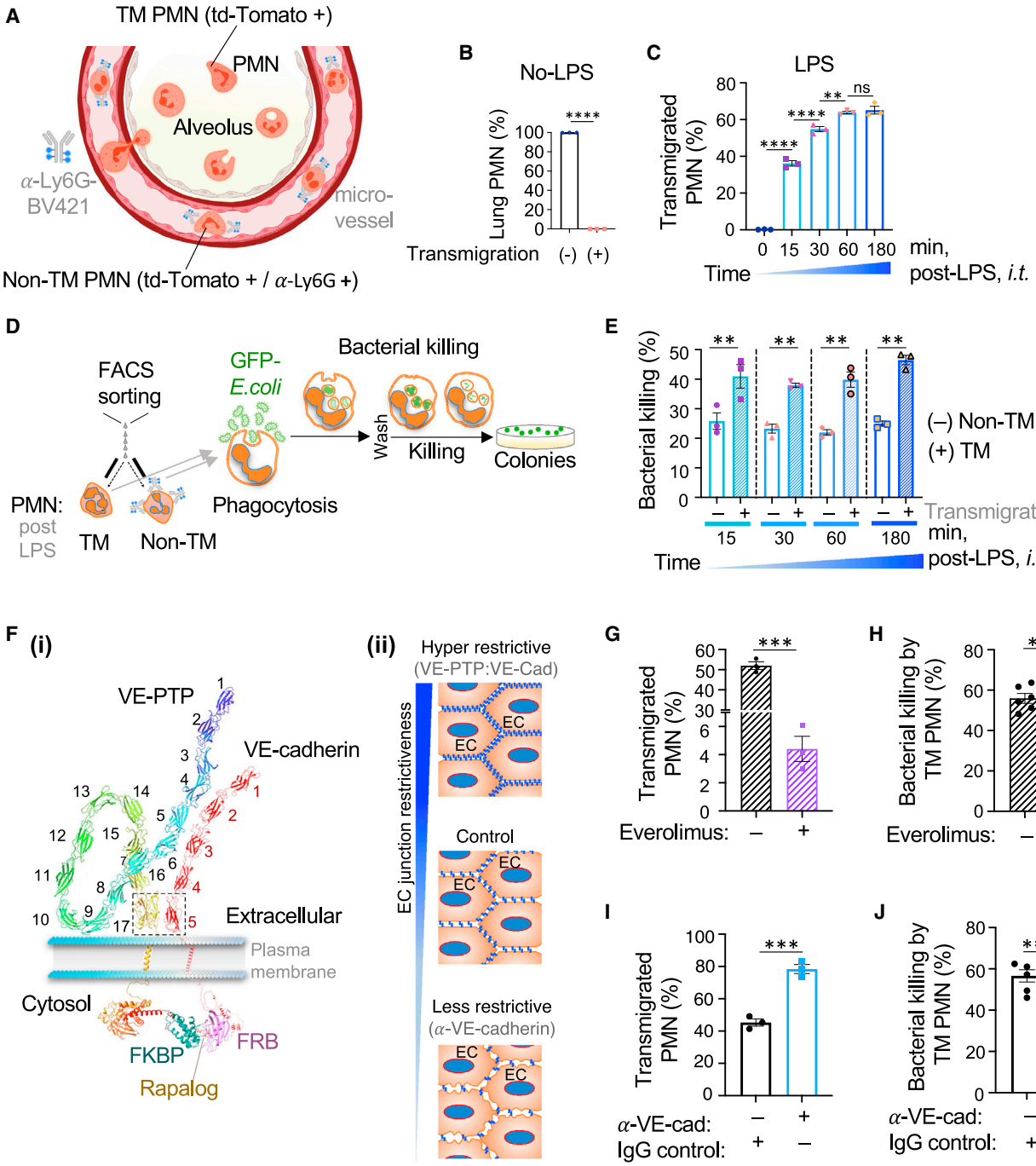

Figure 1. PMN transmigration in endothelial AJs promotes PMN bactericidal activity

(A) Schematic of the method used to separate TM and non-TM PMNs across lung microvessels. All PMNs from *Ly6G*$^{Cre\ td\text{-}Tomato\ +/-}$ mice expressed td-Tomato as shown in Figure S1A. Intravascular PMNs were additionally labeled by α-Ly6G-BV421 antibody injected i.v. 2 min prior to euthanasia. The number of extravasated td-Tomato PMNs relative to intravascular PMNs stained with α-Ly6G-BV421 was calculated to quantify *trans*-vascular PMN migration.

(B and C) Percentage transmigrated (TM) and non-transmigrated (non-TM) PMNs assessed by FACS analysis in naive mice and mice exposed to 5 mg/mL insufflated (i.t.) LPS for different times (as shown in Figure S1C).

(D) Workflow to assess bactericidal activity of TM vs. non-TM PMNs. Flow sorted TM and non-TM lung PMNs were incubated with *GFP-E.coli* for 1.5 h to determine bacteria phagocytosis, and number of live bacteria was determined at 3.5 h after bacteria washout.

(E) Bactericidal activity represented as % of killed GFP-*E.coli* normalized to phagocytosed GFP-*E.coli* (Figure S1F) of TM vs. non-TM lung PMNs obtained at different times post-LPS challenge as in (C). At each time point, TM PMNs induced 2-fold increase in bacterial killing. Data are obtained from 3 mice per group from 3 independent experiments.

(legend continued on next page)

Please cite this article in press as: Mukhopadhyay et al., *trans*-Endothelial neutrophil migration activates bactericidal function via Piezo1 mechanosensing, Immunity (2023), https://doi.org/10.1016/j.immuni.2023.11.007

role of restrictive endothelial junctions in promoting PMN bactericidal function through activation of Piezo1-Nox4 signaling pathway in the PMNs entering tissue. Thus, mechanical activation of Piezo1 expressed in PMNs during their passage through the restrictive space may be a useful therapeutic strategy for treating inflammatory diseases such as acute respiratory distress syndrome (ARDS) through amplifying the PMN bactericidal function.

RESULTS

AJs enhance bactericidal function of transmigrating PMNs

To determine whether transmigration of PMNs via junctions of the endothelial cell monolayer lining blood vessels[33,34,35] is responsible for a PMN phenotype shift, we distinguished between transmigrated (TM) and non-transmigrated (non-TM) PMNs in mice, using the approach in Chiang et al.[36] (Figure 1A). We used genetically targeted Catchup$^{IVM\text{-}red}$ mice co-expressing *Cre* recombinase along with the fluorescent protein td-Tomato under the control of PMN-specific locus Ly6G[37] (Figure S1A). Following insufflation of lipopolysaccharide (LPS) in mice to induce PMN transmigration from lung microvessels into extravascular space, we observed that td-Tomato^{+} PMNs accumulated in both vessels and lung tissue (Figures 1A–1C, S1B, and S1C). The vascular resident non-transmigrating PMNs were intravitally stained with α-Ly6G antibody conjugated to Brilliant-violet (BV421) fluorophore injected intravenous (i.v.) 2 min prior to euthanasia (Figures 1B and S1C). Using fluorescence-activated cell sorting (FACS), we demonstrated that both peripheral blood and lung intravascular PMNs isolated from control mice were positive for td-Tomato stained with α-Ly6G-BV421 antibody (Figures S1C–S1E). Exposure of mice to LPS however increased accumulation of td-Tomato+ PMNs, as evident by the cells that did not stain with α-Ly6G-BV421 antibody (Figures 1C and S1C). The latter staining enabled the distinction between the TM PMN population and the PMNs remaining in microvessels (Figure S1C). Analysis of PMN transmigration in mice exposed to LPS showed that recruitment of PMNs into lung tissue occurred as early as 15 min post-LPS (the earliest time it could be assessed), and the number of PMNs in lung tissue continued to increase over the next 60 min (Figures 1C and S1C).

We next studied *E. coli* clearance via phagosomes in TM PMNs (Figure 1D). Assessment of FACS-sorted lung extravasated PMNs showed that they possessed twice the green fluorescent protein (GFP)-*E. coli* clearance capacity, as compared with non-TM PMN, and unlike non-TM PMN, the response persisted up to 180 min post-LPS (Figure 1E). In contrast, we observed no difference in phagocytosis between TM and non-TM PMNs at any time post-LPS (Figure S1F). The increased clearance of GFP-*E. coli* seen in Figure 1E was unlikely due to inactivation of Ly6G used to detect phagocytosis, since exposure of PMN to α-Ly6G antibody for periods up to 15 min had no effect on antimicrobial activity of PMNs (Figure S1G). These results together show that transmigration of PMN through the restrictive endothelial AJs augmented the bactericidal function of the PMN.

To address genetically the role of restrictiveness of AJs in activating PMN bactericidal function, we enhanced the AJ barrier using a transgenic mouse model[38] expressing an engineered construct containing both VE-cadherin-FK506 and vascular endothelium Protein tyrosine phosphatase (VE-PTP)-FKBP-rapamycin-binding domain (FRB) fusion proteins under the control of the endogenous VE-cadherin promoter (Figure 1Fi). Endothelial junctions became far more restrictive after treatment of mice with the rapamycin analog everolimus that irreversibly stabilized the interaction between VE-cadherin-FK506 and the interacting VE-cadherin-associated protein tyrosine phosphatase VE-PTP-FRB.[38,39] This mechanism of increasing endothelial barrier restrictiveness is based on the described interaction between extracellular (fibronectin type III [FNIII]) domain 17 of VE-PTP and domain 5 (EC-V) of VE-cadherin.[40] Using this model to study the role of increased endothelial barrier restrictiveness on transmigrating PMNs (Figure 1Fii), we observed a markedly reduced number of transmigrating PMNs (Figure 1G), whereas bactericidal function of PMNs exiting the barrier was enhanced (Figure 1H). This finding is consistent with the crucial role of endothelial junctional barrier in promoting PMN bactericidal function. Conversely, the opening of AJs using anti-VE-cadherin-blocking antibody (clone 11D4.1) to make the barrier more permissive[41] increased the number of transmigrating PMNs (Figure 1I) while reducing their bactericidal activity (Figure 1J). The number of phagocytosed bacteria (Figure S1F) was not different between the experimental groups (Figures S1H and S1I), in contrast to their bacterial clearance mechanism (Figures 1H and 1J). In control experiments, we showed that neither treating PMNs with high concentrations of everolimus nor adding supernatant of endothelial monolayers incubated with α-VE-cadherin-blocking antibody independently altered the antimicrobial function of PMNs (Figures S1J and S1K). Together, these experiments showed that the restrictive nature of the endothelial junctions is a key determinant of augmented bactericidal function of TM PMNs.

PMN migration through restricted microfluidic pore system promotes bactericidal function

We next used a microfluidic approach to test whether PMN transmigration via known pore diameters could induce changes in PMN phenotype similar to transmigration in AJs above. PMNs

(Fi and Fii) (i) Model demonstrating the method of increasing the restrictiveness of endothelial AJs through expression of engineered VE-cadherin-FK506 and vascular endothelium Protein tyrosine phosphatase (VE-PTP)-FKBP-rapamycin-binding domain (FRB) fusion proteins in mice as in Broermann[38]; this method stabilized VE-cadherin-VE-PTP interaction and increased junction barrier restrictiveness on treating with the drug everolimus. (ii) Schema of the approaches used to either increase or decrease restrictiveness of AJs.

(G and H) Percent of TM PMNs into lungs (G) and bactericidal activity of TM PMNs (H) in transgenic mice treated with everolimus ("+") or vehicle control ("−"). Bactericidal activity of PMNs transmigrating through restrictive AJs of mice treated with everolimus was greater than control.

(I and J) Percent of TM PMNs into lungs (I) and bactericidal activity of TM lung PMNs (J) of C57B6 mice treated with isotype-matched antibody as well as functional blocking α-VE-cadherin antibody used to disassemble AJs. PMN bactericidal activity was reduced in lungs after α-VE-cadherin antibody-induced opening of AJs. Data are obtained from 3 to 6 mice per group from 3 independent experiments. Additional information is provided as Figure S1.

Please cite this article in press as: Mukhopadhyay et al., *trans*-Endothelial neutrophil migration activates bactericidal function via Piezo1 mechanosensing, Immunity (2023), https://doi.org/10.1016/j.immuni.2023.11.007

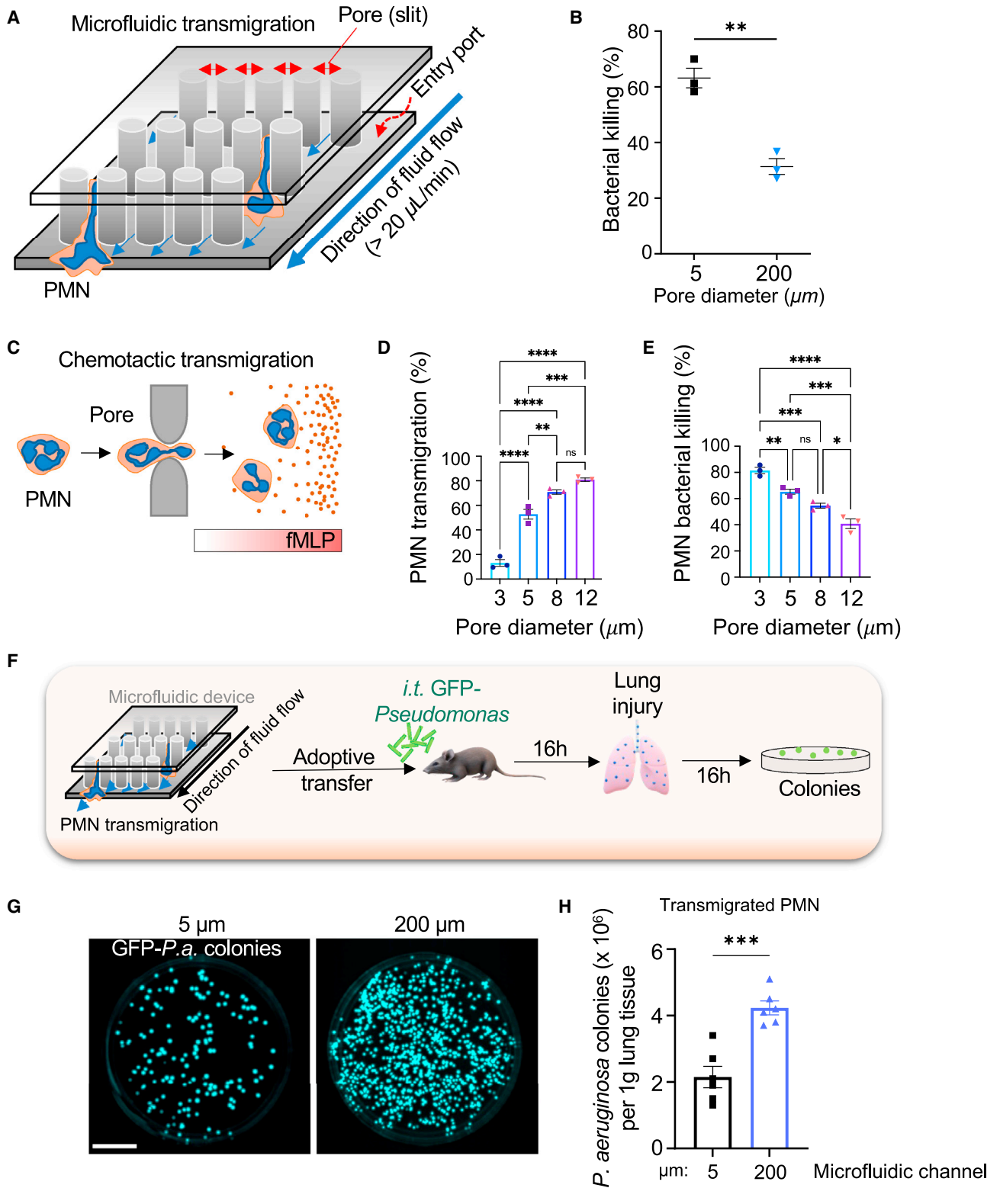

Figure 2. PMN transmigration via restrictive pores in a microfluidic system enhances bactericidal activity of PMN

(A) Design of the microfluidic system containing pores through which PMNs transmigrated.

(B) Murine bone marrow PMNs that transmigrated through 5-μm-diameter pores showed 2-fold greater *E. coli* killing *ex vivo*, as compared with PMNs transmigrating through 200-μm-diameter pores. Data are obtained from 3 independent experiments.

(legend continued on next page)

Please cite this article in press as: Mukhopadhyay et al., *trans*-Endothelial neutrophil migration activates bactericidal function via Piezo1 mechanosensing, Immunity (2023), https://doi.org/10.1016/j.immuni.2023.11.007

were perfused in this system through either 5- or 200-μm-diameter pores (Figure 2A). PMNs passing through 5-μm pores showed enhanced bacterial killing, as compared with PMNs migrating through the 200-μm pores (Figure 2B), whereas no difference was seen in bacterial phagocytosis in either pore dimensions following PMN transmigration (Figure S2A). We next tested whether the chemoattractant N-formyl-methionyl-leucyl-phenylalanine (fMLP)-induced transmigration of PMNs through the Transwell membrane containing pores of different diameters also influenced the antimicrobial activity of PMNs. Results showed that PMN migration across pores in this system was a direct function of the pore diameter (Figure 2D). PMN transmigrating through smaller diameter pores effectively killed *E. coli*, as compared with transmigration through larger pores (Figures 2D and 2E). In control experiments (Figure S2B), PMNs exposed to 1 μM fMLP in the absence of passage through pores showed no such difference in killing of *E. coli*, highlighting the importance of restrictive pores in mediating the bactericidal killing function of PMNs.

To further address the augmented bacterial killing phenotype of TM PMNs, we carried out an adoptive transfer experiment in which these PMNs were instilled intratracheally (i.t.) (Figure 2F). Here, we used murine bone marrow PMNs that had been perfused through either 5- or 200-μm-diameter pores in the microfluidic system. We used a model of pneumonia induced by *Pseudomonas aeruginosa* instillation in lungs[42] and studied changes in bactericidal activity of PMNs that had been pre-exposed to transmigration. We observed that PMNs migrating across 5-μm pores showed improved clearance of *Pseudomonas aeruginosa* from lungs of infected mice, as compared with PMNs that passed through 200-μm gaps (Figures 2G and 2H).

Piezo1 sensing of membrane tension induces calcium signaling in PMNs during *trans*-endothelial migration

As PMNs experience distortion forces during migration across restrictive AJs, we addressed the possible role of the mechanosensor Piezo1, a non-selective Ca^{2+} channel,[43] expressed in PMNs in mediating the PMN phenotype shift. To assess changes in Ca^{2+}, we intravitally imaged Ca^{2+} influx in PMNs during their transmigration phase using the Ca^{2+} indicator GCaMP6f constitutively expressed in PMNs. Using dual-channel two-photon live-cell imaging microscopy, we observed that cyclic cytosolic Ca^{2+} transients in PMNs occurred only during the transmigration phase (Figures 3A–3C; Video S1). The response waned as the cells exited the junctions (Figures 3B and 3C). A similar pattern in cytosolic Ca^{2+} transients was observed in the PMNs migrating across endothelial cells of cremaster venules (Figures S2C–S2E; Video S4), indicating that Ca^{2+} spikes were a generalized response in all transmigrating PMNs. To address whether Ca^{2+} influx observed during PMN transmigration was mediated by Piezo1 mechanosensing, we transfected PMNs derived from HL-60[44] cells with control or Piezo1 short hairpin RNA (shRNA) constructs (Figure S3A). Results showed that Piezo1 depletion in PMNs prevented the Ca^{2+} influx seen in PMNs transmigrating through 5-μm pores (Figures 3D–3F). To address the basis of Piezo1-mediated Ca^{2+} flux, we treated PMNs with thapsigargin, a non-competitive inhibitor of endoplasmic reticulum (ER) Ca^{2+} ATPase (sarcoendoplasmic reticulum calcium ATPase [SERCA] pump) that releases Ca^{2} from ER stores[45] or used the ionophore ionomycin to induce Ca^{2+} entry through the plasma membrane[46] by a Piezo1-independent mechanism. Treatment of PMNs with ionomycin, but not with thapsigargin, enhanced bactericidal function of PMNs (Figure S3B). The latter experiments were carried out under nominally free extracellular Ca^{2+} condition to prevent store-operated Ca^{2+} entry after ER Ca^{2+} depletion (Figure S3B). These results support the central role of plasmalemma Ca^{2+} entry in PMNs during transmigration via the Piezo1 channel as a central signaling mechanism of PMN bactericidal function.

To assess next whether PMNs traversing AJs could generate sufficient tension to activate Piezo1, we used a computational model to determine spatial changes in membrane tension of human PMNs with the mean diameter of 8.5 μm. Membrane tension was found to be increased during the transmigration phase at the sites of PMN contact with junctions (Figure 3G; Video S2). Maximum membrane tension experienced by PMNs was inversely proportional to the pore diameter (Figure 3H) and increased with the total external force needed to push PMNs through junctions (Figure 3H). The total pressure applied to PMNs also increased proportionally to the pore diameter (Figure S2F). The pressure consisted of intracellular force generated by the PMN actomyosin apparatus and the force generated by the hydrodynamic pressure difference between blood vessel and extravascular tissue (Figures 3H and S2F). PMN membrane tension generated by these forces from 0.7 to 1.4 nN/μm was in the range required to gate the Piezo1 channel.[47,48] As shear stress has also been shown to activate Piezo1,[39,49] we determined whether PMNs traversing through the 5-μm pores in the microfluidic system (Figure S2G) encountered sufficient mechanical fluid shear to affect Piezo1 channel opening during the transmigration phase (see STAR Methods for details). We demonstrated migration and squeezing of PMNs through 5-μm pores of the system in real time at 30,000 frames s^{-1} (Video S3). The flow field inside the microfluidic system was used to predict the velocity and shear stress in the channel under given flows (Figure S2H). The maximum fluid shear was estimated to be 191.924 Pa for flow of 20 μL/min, and it was linearly proportional to the flow. Passage of PMNs through this system generated sufficient plasma

(C) Murine bone marrow PMN transmigration through the Transwell system with pore diameters ranging from 3 to 12 μm in response to a gradient of the chemoattractant fMLP.

(D) Percentage of transmigrated PMN through different pore sizes as shown in (C). PMN transmigration is a direct function of pore diameter.

(E) Bactericidal activity of PMNs transmigrated through different pore diameters as in (C). PMN transmigrating through smaller pore augmented bacterial killing. Data are from 3 independent experiments.

(F) Schematic of the adoptive transfer experiment in which mice challenged with GFP-*Pseudomonas aeruginosa* (GFP-*P.a.*) received 1 × 10^6 PMNs through i.t. route.

(G and H) Infected mice adoptively transferred with murine bone marrow-derived PMNs subjected to transmigration through 5-μm-diameter pores (as in A) showed increased clearance of *Pseudomonas aeruginosa*, as compared with control PMNs passed through 200-μm pores. Data are obtained from 6 mice per group from 6 independent experiments. Scale bars, 25 mm. Additional information is provided as Figures S2A and S2B.

Please cite this article in press as: Mukhopadhyay et al., *trans*-Endothelial neutrophil migration activates bactericidal function via Piezo1 mechanosensing, Immunity (2023), https://doi.org/10.1016/j.immuni.2023.11.007

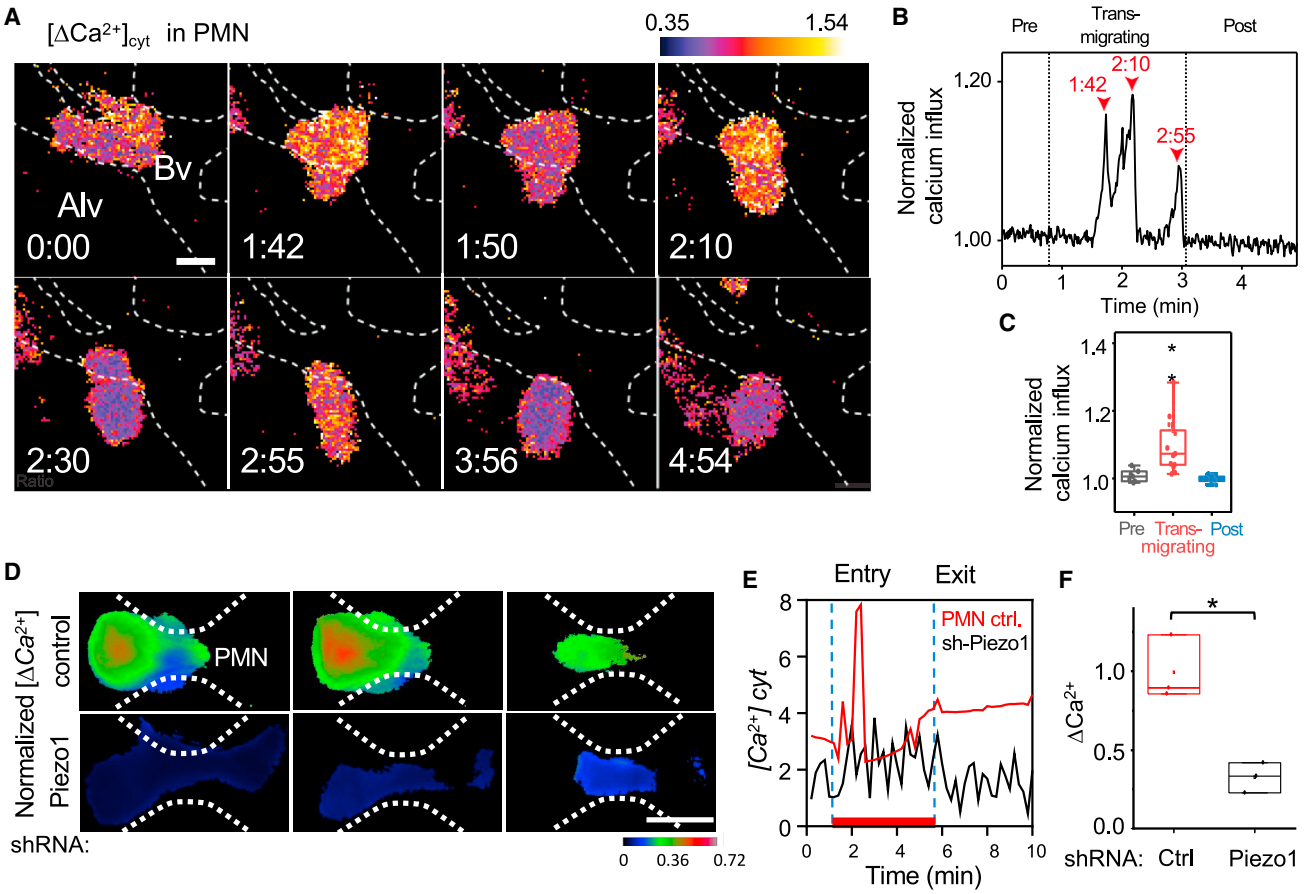

Figure 3. PMN migration through endothelial junctions activates calcium signaling via Piezo1 in PMN

(A) Ca^{2+} transients in PMNs determined by motion-corrected two-photon lung intravital imaging of the Ca^{2+} indicator GCaMP6f (green) before, during, and after PMN transmigration in endothelial AJs of lung microvessels. PMN reporter was td-Tomato expressed under Ly6G promoter (red); endothelial junction labeled by

(legend continued on next page)

Please cite this article in press as: Mukhopadhyay et al., *trans*-Endothelial neutrophil migration activates bactericidal function via Piezo1 mechanosensing, Immunity (2023), https://doi.org/10.1016/j.immuni.2023.11.007

membrane tension in the range[43,44] required to gate Piezo1 (Figures S2I and S2J; Video S5).

Piezo1 in transmigrating PMNs activates bactericidal function

To address whether Piezo1 activation in the PMN plasma membrane was required for enhanced PMN bactericidal function, we treated freshly isolated human peripheral blood PMNs with the activator of Piezo1, Yoda1[50] (Figure 3I). Both activation of Piezo1 with Yoda1 and mechanical forces of microfluidic system during PMN migration across 5-μm pores increased bactericidal activity, as compared with control PMNs (Figure 3I). However, activation of Piezo1 did not alter phagocytosis of bacteria (Figure S3C). Furthermore, adoptive i.t. transfer of murine bone marrow PMNs pretreated with Yoda1 improved the clearance of *Pseudomonas aeruginosa* from lungs of i.t. 10^6 GFP-expressing *Pseudomonas aeruginosa*-infected mice (Figures 3J and 3K).

To genetically study the role of Piezo1 activation in transmigrating PMNs in bacterial killing, we generated homozygous PMN-restricted *Piezo1* mutant mice (*Piezo1*$^{\Delta PMN}$) by crossing *Piezo1*$^{fl/fl}$ with Catchup$^{IVM\text{-}red}$ mice containing Ly6G-Cre (Figures S3D and S3E). Deletion of *Piezo1* in PMNs had no significant effect on the PMN number in peripheral blood (Figure S3F) and did not alter maturation of bone marrow PMNs (Figures S3G and S3H). In *Piezo1*$^{\Delta PMN}$ mice instilled with i.t. 10^6 GFP-expressing *Pseudomonas aeruginosa* (Figures 4A–4K), we observed a greater number of *Pseudomonas* colonies in lungs (Figures 4A–4D) as well as augmentation of inflammatory lung injury (Figures 4E and 4F) and increased mortality (Figure 4G), as compared with wild type (WT). These results show the obligatory role of PMN-expressed Piezo1 in regulating the PMN bactericidal function.

To address the basis of Piezo1-mediated increase in bactericidal activity, we analyzed factors such as the distance between *Pseudomonas aeruginosa* foci and PMNs in infected lungs. We observed that deletion of *Piezo1* in PMNs did not alter their ability to phagocytize bacteria (Figures 4H–4J andS3I), whereas Piezo1-deficient PMNs localized closer to the bacteria, as compared with control PMNs (Figures 4H and 4J). Notably the number of PMNs with phagocytized bacteria was similar between groups (Figure S3I). Although lungs of *Piezo1*$^{\Delta PMN}$ mice contained more PMNs (Figure S3J), their proportion to *Pseudomonas aeruginosa* was reduced, as compared with lungs of control mice (Figure 4K). Furthermore, *Piezo1* deletion in PMNs had no effect on survival of TM lung PMNs cultured *ex vivo* (Figure S3K). Another important phenotype of *Piezo1*$^{\Delta PMN}$ mutant mice was their inability to form neutrophil extracellular traps (NETs) in response to *Pseudomonas aeruginosa* challenge (Figure S3L). We also analyzed the effects of Piezo1 deficiency on PMN migration in lung tissue, following the onset of inflammatory lung injury induced by insufflated LPS (Figures 4L–4N). Here, we distinguished TM and non-TM PMN by chase labeling of lung tissue PMNs with α-Ly6G-BV421 antibody before carrying out intravital imaging (see STAR Methods). Analysis of migratory velocity of extravascular PMNs (Ly6G-Alexa594+) (Figure 4L) showed that deletion of *Piezo1* in PMNs reduced the velocity of PMNs from 3 μm/min of control PMNs to 0.8 μm/min (Figures 4M and 4N). Together, these data showed that Piezo1 expression in PMNs is crucial in mediating bactericidal, NET forming, and migratory functions of PMNs.

Piezo1 signaling in transmigrating PMNs activates immune regulatory genes

We carried out a transcriptome analysis of TM vs. non-TM PMNs in mice to identify possible Piezo1-dependent genomic alterations that could explain enhanced bactericidal function of TM PMNs. TM and non-TM PMNs showed distinct transcriptomic profiles in WT and *Piezo1*$^{\Delta PMN}$ mice (Figures 5A–5F; Table S1 showing all differentially expressed genes [DEGs]). We found NOX4, the constitutively active isoform that generates hydrogen peroxide in the phago-lysosomal compartment,[30,31,32] was upregulated in TM PMNs but reduced in TM PMNs of *Piezo1*$^{\Delta PMN}$ mice (Figures 5E and 5F), suggesting the relationship between Piezo1 activation and *Nox4* expression. The role of NOX4 was thus specifically addressed as described below.

To identify whether Piezo1 activation improved PMN host-defense function, we used ingenuity pathway analysis (Figures 5G andS4; Table S1). The most altered bactericidal response pathways included acute phase response signaling, pathogen

anti-PECAM1 antibody (blue). Real-time data is supplied as Video S1. Scale bars, 0.3 mm/pixel; image capture rate, 2 s/frame. The color scheme shows blue as the lowest and yellow as highest increase in cytosolic [Ca^{2+}]. The dotted line shows the lung capillary wall with a monolayer of endothelial cells. Bv, blood vessel; Alv, alveolus. Time is in min and s. Scale bars, 5 μm.

(B) Changes in cytosolic [Ca^{2+}] during PMN transmigration in (A). Arrowheads indicate Ca^{2+} spikes and corresponding times during PMN transmigration.

(C) Quantification of Ca^{2+} peaks normalized to baseline fluorescence prior to transmigration. Data are presented for 5 transmigration events observed in 5 mice. The boundaries of the boxplot indicate the 25th and 75th percentiles; whiskers show 1.5× interquartile range; median is shown by the straight line.

(D–F) Time-lapse images of Fluo4 in control and shRNA-silenced Piezo1 PMNs (HL-60 derived) migrating through 5-μm pores of the microfluidic system. Scale bars, 8 μm. Individual Fluo4 tracings (E) and quantifications (F) demonstrating changes in cytosolic [Ca^{2+}] in control and Piezo1-deleted PMNs in (D). The boundaries of the boxplot indicate the 25th and 75th percentiles. The median is shown by the straight line. Data are obtained from 3 independent experiments.

(G and H) Finite element simulations of PMNs (8.5 μm in diameter) transmigrating through the restrictive AJs. (G) A cross-sectional view of coupled finite element and boundary element simulations of predicted tension and pressure on PMN plasma membrane during passage through a pore with diameter of 2.4 μm under external force of 1.8 nN, which is about 5 times the minimal external force required to push the PMN through the pore. The color maps show color-coded ranges for PMN membrane tension and pressure. (H) Graph demonstrating maximum tension values at the PMN membrane (dark blue and cyan) and activation probability of the tension sensor Piezo1 (brown and pink) during PMN migration as a function of pore diameter under two different external forces, the minimal critical external force (dark blue and brown) and five times (5×) the minimal external force (cyan and pink) needed for PMNs to pass through pores.

(I) Percent of *E. coli* killed by human PMNs cultured under static condition and treated with vehicle control or Yoda1 to induce Piezo1 activation or post-transmigration through 5-μm pores of the microfluidic system. Data are obtained from 3 independent experiments. The response was increased by Yoda1 treatment to the same degree as passing PMNs through 5-μm pores.

(J and K) Mice that received i.t. adoptive transfer of 10^6 murine bone marrow-derived PMNs pretreated with Yoda1 showed marked improvement of *Pseudomonas aeruginosa* clearance at 16 h post-i.t. instillation of 10^6 colony-forming unit (CFU) bacteria per mouse, as compared with vehicle control. Data were obtained from 5 to 6 mice per group from 3 independent experiments. Additional information is provided as Figures S2C–S2J and S3A–S3E.

Please cite this article in press as: Mukhopadhyay et al., *trans*-Endothelial neutrophil migration activates bactericidal function via Piezo1 mechanosensing, Immunity (2023), https://doi.org/10.1016/j.immuni.2023.11.007

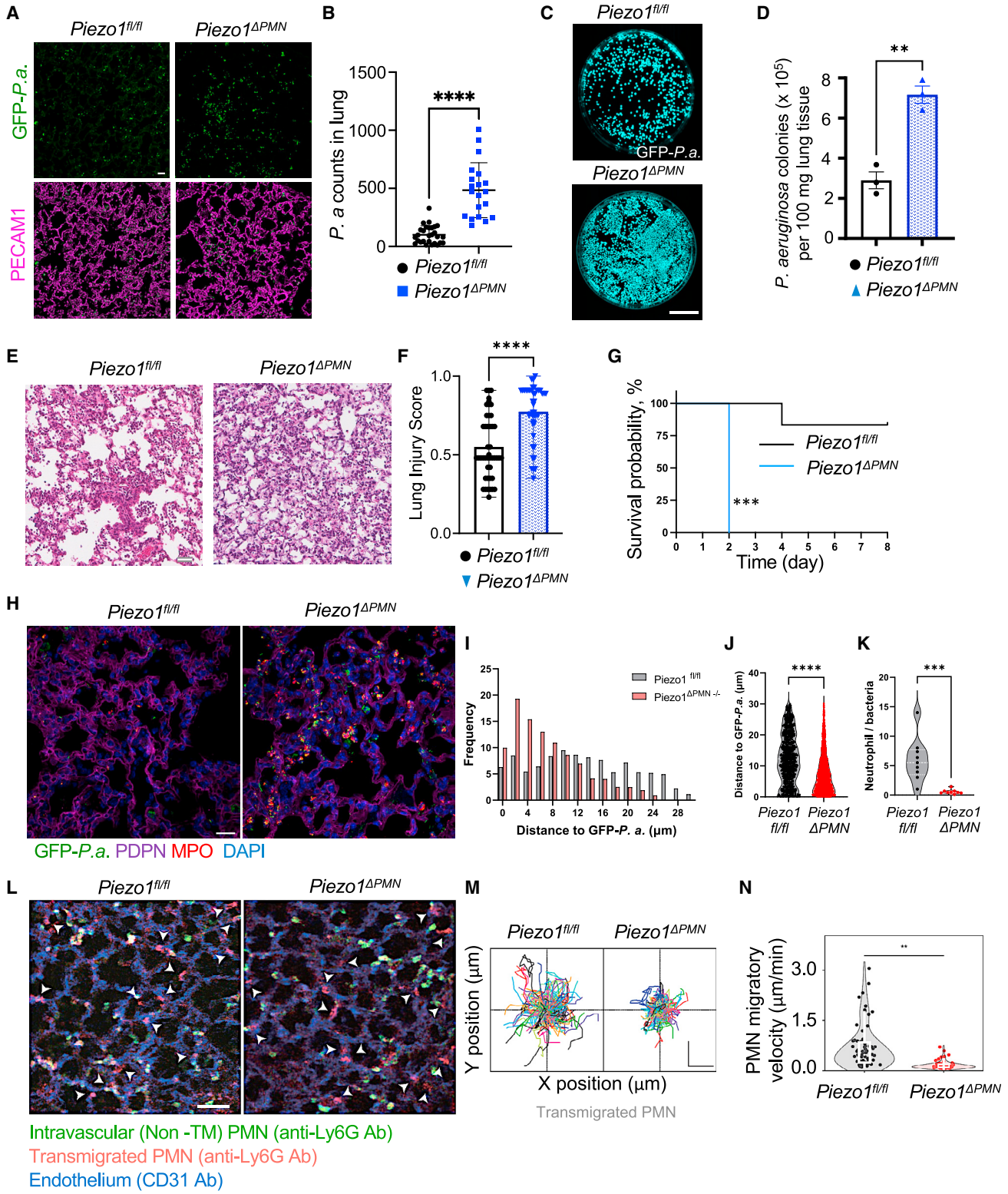

Figure 4. Activation of Piezo1 in transmigrated PMN increases bactericidal activity

(A–K) Genetic deletion of *Piezo1* in PMNs augmented lung infection due to diminished antimicrobial activity of PMNs. (A) Representative images of lung sections stained for GFP-*Pseudomonas aeruginosa* (green) and PECAM-1 (magenta) and (B) quantification of GFP-*Pseudomonas aeruginosa* counts in lung tissue of control (*Piezo1*$^{fl/fl}$) and PMN-specific Piezo1-deleted (*Piezo1*$^{\Delta PMN}$) mice challenged with 10^6 CFU bacteria per mouse for 12 h. Scale bars, 20 μm. (C) Images of GFP-expressing *Pseudomonas aeruginosa* colonies grown on agar plates as in (A) and (B). Scale bars, 25 mm. (D) Quantification of data in (C). Data were obtained

(legend continued on next page)

Please cite this article in press as: Mukhopadhyay et al., *trans*-Endothelial neutrophil migration activates bactericidal function via Piezo1 mechanosensing, Immunity (2023), https://doi.org/10.1016/j.immuni.2023.11.007

recognition receptors, communications between innate and adaptive immunity, Hif1α, and Ca^{2+} signaling (Figure 5G). The predicted association between Piezo1-induced Ca^{2+} signaling, Hif1α signaling, and *Nox4* expression in TM PMNs suggests a role for Piezo1-mediated Ca^{2+} influx in Hif1α stabilization,[51] which may transcriptionally upregulate the phago-lysosomal protein NOX4[51] causing enhanced bacterial killing. This prediction was experimentally addressed as described below.

We observed that the inflammatory and Ca^{2+} signaling pathways in TM PMNs of *Piezo1*$^{\Delta PMN}$ mice were not upregulated (Figures S4D, S4G, and S4F). Analysis showed the downregulation of genes linked to Hif1α signaling in TM *Piezo1*$^{\Delta PMN}$ PMNs (Figure S4D), suggesting that Piezo1 activation was required for the upregulation of Hif1α target genes. We also found that Hif1α was stabilized within minutes of Piezo1 activation (Figure S4H) and that small interfering RNA (siRNA)-mediated depletion of *Hif1α* abrogated the Piezo1-dependent enhancement of bacterial killing (Figures S4I and S4J).

We next determined, using multi-colored spectral flow cytometry, whether differential expression of PMN surface markers was altered in TM vs. non-TM PMNs (Figures 5H–5K and S5). TM PMNs of WT mice showed upregulation of *Mme* (CD10) (Figures 5I and S5A), the gene encoding membrane metalloproteinase. TM PMNs also showed upregulation of CD47, also known as integrin-associated protein (Figures 5K and S5A). These changes were however reduced in PMNs of *Piezo1*$^{\Delta PMN}$ mutant mice (Figures 5I and 5K). TM PMNs of *Piezo1*$^{\Delta PMN}$ mice also showed significant upregulation of transcript and surface protein expression of CXCR4, the C-X-C chemokine receptor type 4 (Figures 5H, S5A, and S5B), known to promote chemotaxis and suppress cell death.[52] We did not observe significant change in surface expression of CD11b in TM PMNs from WT mice; CD11b surface expression was reduced in TM PMNs of *Piezo1*$^{\Delta PMN}$ mice (Figure 5J). These data together showed that TM of PMNs activated a range of transcriptional programs, some of which were altered by deletion of Piezo1. The results support the important role of TM of PMN in activating multiple Piezo1-dependent genomic programs that alter the function of transmigrating cells.

Upregulation of *Nox4* in transmigrating PMNs is required for bactericidal function

As our transcriptome data above suggested that Piezo1 induced upregulation of Nox4 in TM PMNs (Figures 5E and 5F), we addressed whether the function of Piezo1-NOX4 signaling was a critical requirement for activation of the TM PMNs and for increased bactericidal function of these cells. Like other NADPH oxidases,[20] NOX4 mediates bacterial killing via ROS generation. Analysis of *Nox* isoforms in TM vs. non-TM PMNs challenged with LPS showed that mRNA expression of *Nox2* and *Nox4* was upregulated in TM PMNs whereas *Nox1* was downregulated (Figure 6A). Critically, genetic ablation of *Piezo1* in PMNs interfered only with *Nox4* upregulation in the TM PMNs (Figure 6B). Furthermore, activation of Piezo1 with Yoda1 increased *Nox4* mRNA in PMNs as early as 30 min post-treatment (Figure 6C). We also observed increased NOX4 protein expression in PMNs stimulated with Yoda1 (Figure 6D). NOX4 protein expression was upregulated in HL-60-derived PMNs that TM in 5-μm pores in response to fMLP chemotactic gradient (Figure 6E). Increase in NOX4 expression was significantly less in PMNs transmigrating through larger 12-μm-diameter pores and in Piezo1-depleted PMNs (Figure 6E). In other control experiments, fMLP exposure of PMNs grown in suspension or non-TM PMNs showed no upregulation of NOX4 (Figure 6E).

As NOX4 appeared to be important in bacterial killing by TM PMNs, we next studied NOX4 by tagging it with GFP. GFP-NOX4 localized to the cup-shaped invaginations of the plasma membrane of HL-60-derived PMNs (Figures S6A and S6B) and co-localized with F-actin cytoskeleton (Figure S6C). Upon incubation with *Pseudomonas aeruginosa*, NOX4-GFP was seen within the early and late phagosomes as well as phagolysosomes (Figure S6A, S6B, and S6D). To address the specific role of NOX4 in Piezo1-activated bactericidal function in TM PMNs, we treated PMNs with a dual inhibitor of NOX1 and NOX4, GKT137831,[53] or depleted NOX4 using siRNA in HL-60-derived PMNs (Figures 6F, 6G, and S6E). Reduction in NOX4 expression and function reduced the bactericidal activity of PMNs transmigrating through the 5-μm pores (Figures 6F and 6G).

To compare *in vivo* bactericidal activity in lung tissue PMNs of control (*Nox4*$^{fl/fl}$) and homozygous *Nox4*-ablated (*Nox4*$^{\Delta PMN}$) mice (see STAR Methods for details), we exposed mice to 10^6 GFP-expressing *Pseudomonas aeruginosa* and observed crucially that deletion of *Nox4* in PMNs increased the number of *Pseudomonas* colonies in lungs (Figure 6H and 6I). Inhibition of NOX4 with GKT137831 in WT murine bone marrow PMNs perfused through 5-μm pores of the microfluidic system also reduced the clearance of *Pseudomonas aeruginosa* from lungs of infected recipient mice, similar to results seen in Piezo1-deficient PMNs

from 3 mice per group from 3 independent experiments. (E and F) Histopathological assessment of lung injury induced by *Pseudomonas aeruginosa* in *Piezo1*$^{\Delta PMN}$ vs. control mice. Representative images of H&E-stained lung tissue from 3 independent experiments (E) and lung injury scores (F) of mice as in (A) and (B). Scale bars, 20 μm. (G) Survival rates of mice challenged with i.t. 10^6 CFU *Pseudomonas aeruginosa* per mouse. Genetic deletion of Piezo1 in PMNs markedly enhanced mortality. Data were obtained from 9 mice per group from 3 independent experiments. (H–K) Genetic deletion of Piezo1 in PMNs reduced PMN-to-bacteria ratio. (H) Representative images of lung sections stained for GFP-*Pseudomonas aeruginosa* (green) and podoplanin (PDPN, magenta) from 3 independent experiments were used for tissue architecture assessment, PMN marker myeloperoxidase (MPO, red), and 4′,6-diamidino-2-phenylindole (DAPI, blue). Scale bars, 20 μm. (I–K) Histogram distribution (I) and mean distance (J) between PMN and GFP-*Pseudomonas aeruginosa* in lung tissue; and PMN-to-bacteria ratio (K) in lungs of control (Piezo1$^{fl/fl}$) and PMN-specific *Piezo1*-deleted (*Piezo1*$^{\Delta PMN}$) mice as in (A) and (B).
(L–N) Genetic deletion of *Piezo1* in PMNs reduced migratory velocity of PMNs in lung tissue. (L) two-photon microscopic images of lung tissue PMNs of control (Piezo1$^{fl/fl}$) and PMN-specific *Piezo1*-deleted (*Piezo1*$^{\Delta PMN}$) mice 4 h after challenge with insufflated LPS. Total lung intravascular and tissue PMNs (red) were detected by i.v. staining of PMNs with Alexa594-labeled α-Ly6G antibody before LPS insufflation. Intravascular PMNs (green) were stained with BV421-labeled α-Ly6G antibody prior to intravital imaging. Endothelium (blue) was stained with α-CD31 antibody. Arrow heads show transmigrated PMNs in extravascular tissue. Scale bars, 50 μm. (M and N) PMN migratory trajectory (M) and PMN migratory velocity (N) of transmigrated PMNs. *Piezo1*$^{\Delta PMN}$ PMNs showed reduced migration velocity, which was coupled to reduced bacteria killing as shown in (A)–(D) and (K). Scale bars, 20 μm. Data are obtained from 3 mice per group from 6 independent experiments. Additional information is provided as Figure S3.

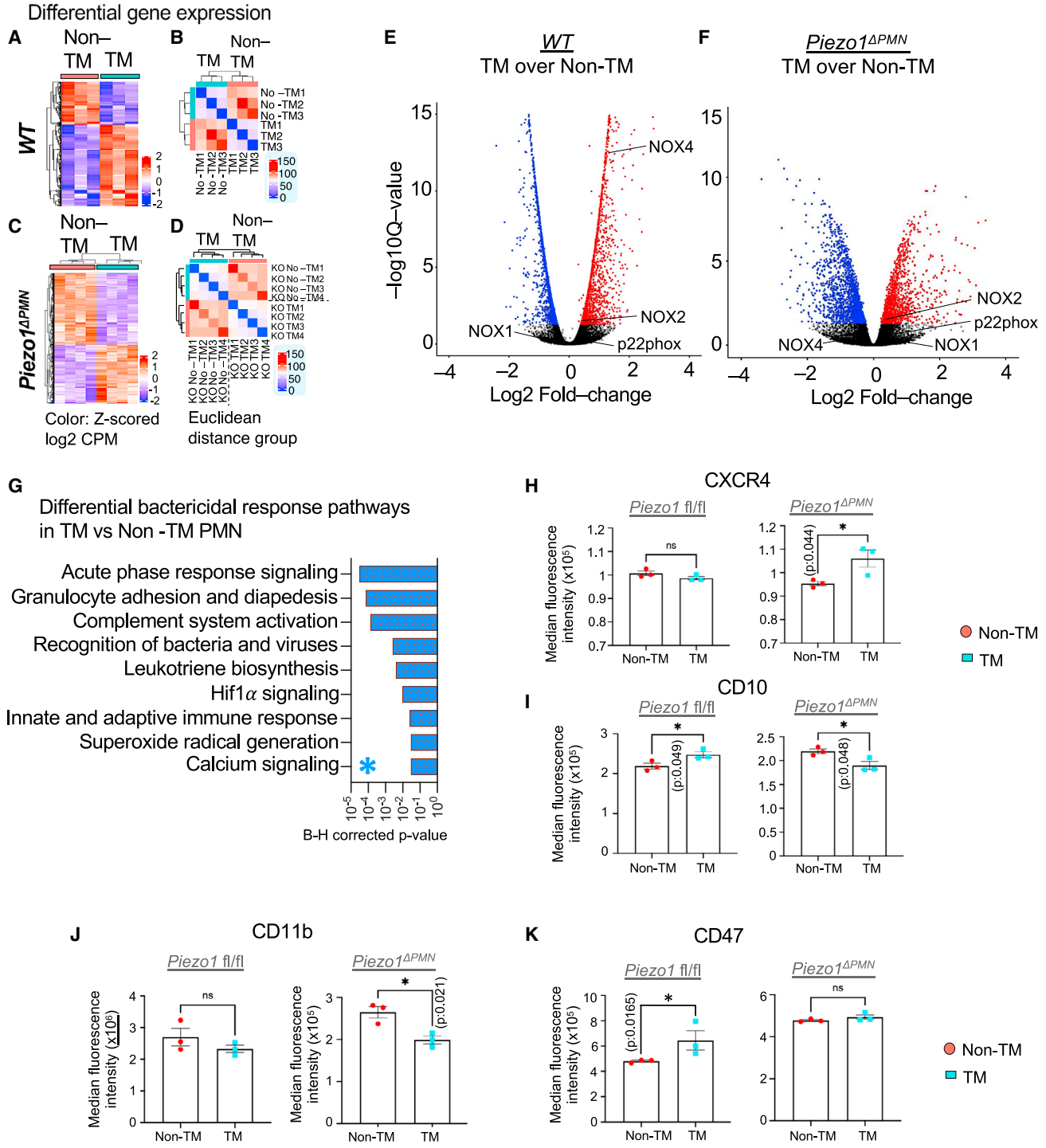

Figure 5. Genetic analysis of transmigrated and non-transmigrated PMNs in lungs

(A–D) RNA-seq analysis of transmigrated vs. non-transmigrated lung PMNs of control (A and B) and PMN-specific Piezo1 mutant (*Piezo1*$^{\Delta PMN}$) mice (C and D). See Table S1 for details. (A and C) Heatmaps of gene expression profiles of non-transmigrated vs. transmigrated PMNs in lungs of control mice and LPS insufflated mice as in Figures 1A and 1B. (B and D) Sample-to-sample distance matrix with color intensity representing Euclidean distance in the gene expression space. Data were obtained from 4 mice per group from 3 independent experiments.

(E and F) Volcano plots showing the overall changes in gene expression in wild-type and *Piezo1*$^{\Delta PMN}$ PMNs as a function of transmigration. NOX4 was upregulated in transmigrated wild-type PMNs, as compared with *Piezo1*$^{\Delta PMN}$ PMN.

(G) The most significant bactericidal pathways derived from IPA analysis are shown (see Table S1 for further details). Hif1α and Ca^{2+} signaling pathways are among the most altered pathways in *Piezo1*$^{\Delta PMN}$ PMNs.

(legend continued on next page)

Please cite this article in press as: Mukhopadhyay et al., *trans*-Endothelial neutrophil migration activates bactericidal function via Piezo1 mechanosensing, Immunity (2023), https://doi.org/10.1016/j.immuni.2023.11.007

(Figures S6F and S6G). Inhibition of NOX4 in Piezo1-deficient PMNs had no additive effect (Figures S6F and S6). Altogether, these data show that Piezo1 enhance PMN host-defense function through upregulation of NOX4. Furthermore, TM PMNs are shown to generate augmented ROS via NOX4 as a function of mechanosensing by Piezo1 during the phase of PMN transmigration (Figure 6J).

DISCUSSION

PMN function is driven by multiple factors including mechanical stimulation and chemoattractants that induce PMN activation and lead to killing of bacteria and other pathogens.[54,55] Activation of PMNs is thus essential for their fundamental host-defense function. Here, we assessed alterations in PMN function induced by mechanical stimuli during the transmigration phase of PMNs through endothelial AJs. This transmigration event is the initial step in activating PMN host-defense system as PMNs breach the vascular endothelial barrier and reach the site of infection.[7,12,56,57] The AJs form pores in the nanometer range, a defining characteristic of all continuous microvascular endothelia,[58] through which PMNs extravasate in response to chemotactic signals into infected tissue. We have described the fundamental role of AJs in re-programming the PMN bactericidal function during *trans*-endothelial migration as was evident by the inverse relationship between restrictiveness of the endothelial junctional barrier and the activation of the bactericidal function of the PMNs entering tissue.

Our results raise the question of relevance of such a PMN transmigration event. Breakdown of AJs due to inflammatory injury and release of permeability-increasing mediators compromise the restrictiveness of AJs,[58] which as shown control the PMN activation state. This was evident in studies in which the restrictiveness of endothelial barrier was genetically increased by forcing the interaction of VE-cadherin, the primary adhesive protein of AJs, and its partner VE-PTP that normally binds VE-cadherin to stabilize VE-cadherin homotypic interaction to restrict the barrier.[40,59] We observed decreased transmigration of PMNs in these mice, but the TM PMNs mounted an intense bactericidal response, as compared with PMNs migrating across looser endothelial junctions. Our results are consistent with observations showing that influx of PMNs into tissue via open or injured junctions did not effectively kill bacteria,[60,61] as opposed to PMNs transmigrating via normal junctions.[41] These results help to explain the pathogenic role of PMNs in mediating tissue injury during inflammatory disease such as ARDS associated with severe disruption of AJs, resulting in augmented tissue PMN accumulation.[62] Our findings also raise the conundrum that severity of leakiness of endothelial junctional barrier in inflammatory diseases reduces bacterial killing, such that PMNs become less effective bactericidal cells when their function is most required.

The present observations revealed the requisite role of the mechanosensor Piezo1, localized in the PMN membrane, in mediating the effects of "squeezing" of PMNs during the transmigration phase and in increasing bactericidal efficacy. Computational modeling showed that transmigrating PMNs experienced plasma membrane tension in endothelial AJs from 0.7 to 1.4 nN/ μm, well in the range required to gate the Piezo1 channel.[47,48] Our central conclusion is that PMN transmigration through restrictive AJs induced the PMN bactericidal phenotype through Piezo1. Piezo1 sensing of tension was required to reprogram the extravasating PMNs and augment their bactericidal function.

Since Ca^{2+} signaling regulates multiple functions of PMNs,[63] we determined, using two-photon intravital microscopy *in vivo*, whether Ca^{2+} changes occurring via Piezo1 gating were responsible for the shift in PMN phenotype. Data here showed tri-shoulder Ca^{2+} transients during PMN passage across endothelial junctions of lung capillaries. Ca^{2+} transients were not seen during the initial adhesion of PMNs to the endothelium or the PMN exit phase. The site of highest Ca^{2+} signal intensity did not correlate with maximum membrane tension seen at the PMN bottleneck region. Although the mechanism is not clear, it is possible that Piezo1 was spatially restricted to the rear to establish rear-front polarity during PMN transmigration or that Piezo1 was activated by intracellular pressure that also increased in the rear as PMNs crossed AJs. This may be also the result of an initial phase of Ca^{2+} entry occurring via Piezo1, which triggers other Ca^{2+} release pathways such as via Ca^{2+}-induced-Ca^{2+}-release (CICR) channel[64,65] or cyclic-AMP (cAMP)-potentiated release.[66] To reinforce these findings seen during *trans*-endothelial PMN migration, we also found similar Ca^{2+} waves in the microfluidic transmigration system, suggesting that the restrictiveness of the junctional barrier was the central cause of Piezo1-dependent Ca^{2+} influx. Piezo1 activation was crucial in mediating the Ca^{2+} influx response, since Piezo1 deletion in PMNs prevented the Ca^{2+} transients seen in transmigrating PMNs.

Piezo1 activation in lung macrophages, unlike PMNs, has been shown to enhance their phagocytosis capacity.[51] In contrast to lung macrophages, the primary effect of Piezo1 in PMNs was enhancement of bacterial killing function. We showed this to be an obligatory mechanism for the PMN host-defense function, since genetic ablation of *Piezo1* in mouse PMNs reduced bactericidal function, and the mice showed increased susceptibility to bacterial infection. Furthermore, the activation of Piezo1 signaling in PMN through adoptive transfer experiments provided therapeutic advantage even in the face of disrupted AJs seen in inflammatory lung injury. Therefore, the present results demonstrate an essential role of Piezo1 expression and activation in PMNs as central to promoting the resolution of bacterial pneumonia.

The PMN nucleus is sufficiently deformable to enable migration through the endothelial junctional barrier, but it cannot be deformed to the extent that it releases DNA and histones, leading to wholesale formation of extracellular traps (NETs).[67,68] PMN nuclei are likely preserved during migration through AJs as the result of composition of the nuclear lamina, a flexible meshwork composed of intermediate filaments woven from type A and type B lamin proteins adjacent to the inner nuclear membrane.[69]

(H–K) Changes in protein-level expression of cell surface markers CXCR4 (H), CD10 (I), CD11b (J), and CD47 (K) in control and *Piezo1*$^{\Delta PMN}$ PMNs upon transmigration as assessed by spectral flow cytometry. Compared with control, the surface expression of CD47 and CD10 were reduced in transmigrated *Piezo1*$^{\Delta PMN}$ PMNs. Results are shown as mean fluorescence intensity. Data are obtained from 3 mice per group. Additional information is provided as Figures S4 and S5.

Please cite this article in press as: Mukhopadhyay et al., *trans*-Endothelial neutrophil migration activates bactericidal function via Piezo1 mechanosensing, Immunity (2023), https://doi.org/10.1016/j.immuni.2023.11.007

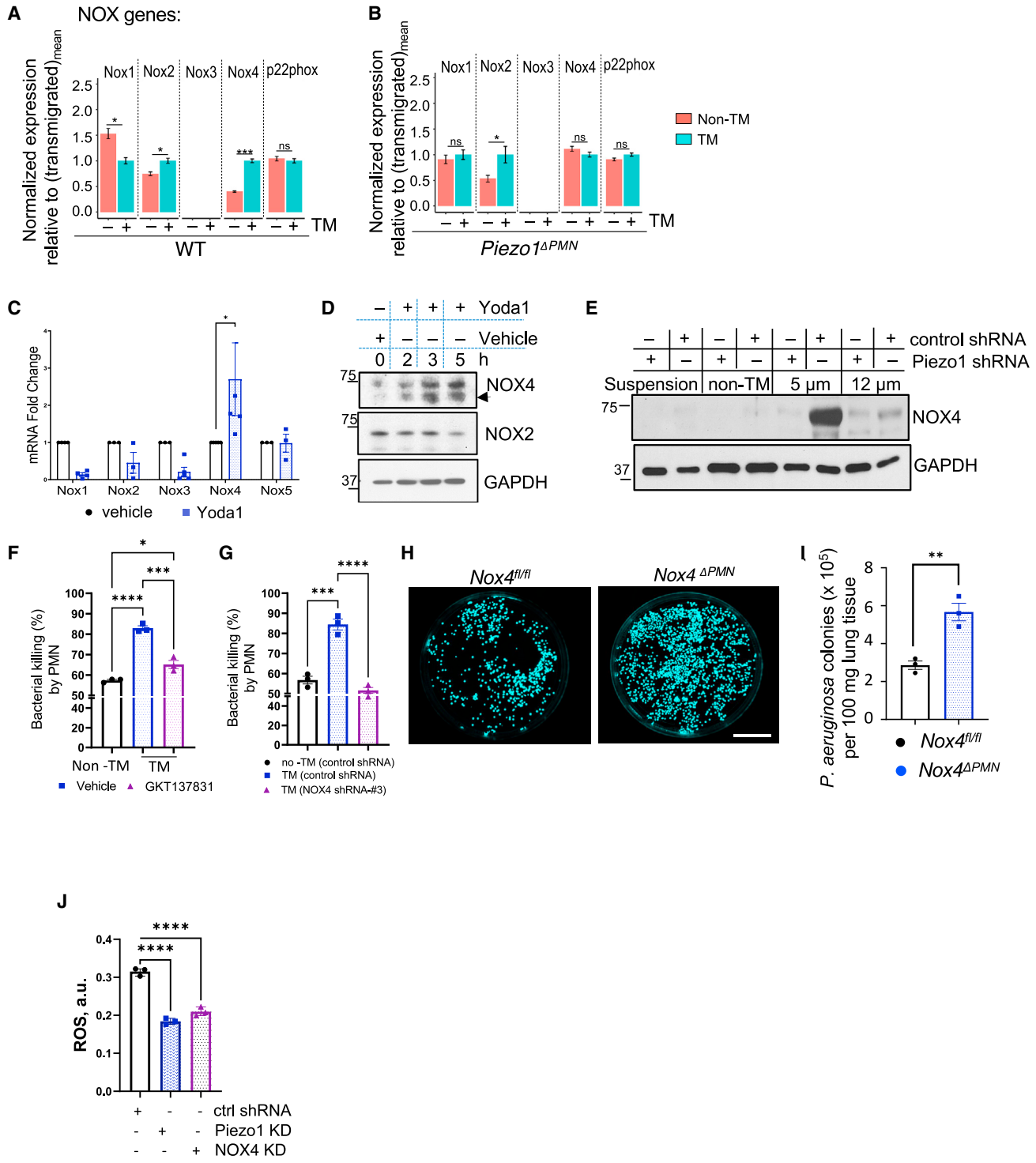

Figure 6. Piezo1 upregulates Nox4 expression to activate bactericidal activity of transmigrated PMN

(A and B) Changes in expression of NOX isoforms in transmigrated vs. non-transmigrated lung PMNs from control (A) and *Piezo1*$^{\Delta PMN}$ PMNs (B), as in Figure 5A, as assessed by RNA-seq analysis (details in Table S1). Increase in NOX4 expression was greater relative to NOX2 in the transmigrated PMNs of control but not of *Piezo1*$^{\Delta PMN}$ mice.

(C) Yoda1 treatment of freshly isolated human PMNs showed increased NOX4 mRNA expression as early as 30 min. Data were obtained from 5 healthy donors from 5 independent experiments.

(D) Western blot showing time course of NOX2 and NOX4 expression in human PMNs treated with Yoda1. Yoda1 increased only NOX4 protein expression.

(legend continued on next page)

However, NET formation did occur in WT mice, but it was reduced in *Piezo1*$^{\Delta PMN}$, suggesting that the forces to which PMNs are exposed during transmigration make them susceptible to NETosis.

Transcriptomic analysis showed that transmigration activated multiple host-defense transcriptional programs in PMNs, and crucially, that these were inhibited by deletion of Piezo1. We also observed impaired upregulation of genes comprising the Ca^{2+} signaling pathway in the TM *Piezo1*$^{\Delta PMN}$ PMNs, as compared with WT PMN. In addition, TM PMNs showed HIF1α-dependent expression of the NADPH oxidase isoform NOX4 gene in *Piezo1*$^{\Delta PMN}$ PMNs, suggesting that NOX4 functions as an effector of Piezo1 signaling downstream of HIF1α stabilization. Bacterial killing induced by TM PMNs required Piezo1 activation and NOX4 expression and was inhibited by HIF1α deletion. While Hif1α signaling has been shown to induce NOX4 transcription,[70] the present study invokes the role of Piezo1 in signaling Hif1α-dependent expression of NOX4. NOX4 is localized in the cup-shaped invaginations of the plasma membrane, specifically in phagosomes and phagolysosomes of PMNs.[30] In contrast, NOX2 is rapidly assembled as an active protein complex that delivers superoxide into the phagosomal lumen.[24,25] NOX4 generates hydrogen peroxide[30,31,32] and thus may have a specialized bactericidal role in phagosomal oxidation and acidification, as compared with NOX2. These results provide insights into the obligatory Piezo1-dependent NOX4 expression and heightened ROS production in mediating the phenotypic switch in transmigrating PMNs into more potent bactericidal cells in tissue.

Piezo1 as a channel permitting Ca^{2+} may itself induce stabilization of Hif1α by the Ca^{2-}/calmodulin-dependent serine/threonine phosphatase, calcineurin,[71] leading to NOX4 transcription in TM PMNs. We cannot rule out the alternate possibility that tissue hypoxia such as encountered during inflammation[70] may also activate NOX4 expression independent of Piezo1 through direct Hif1α-NOX4 signaling. Transcriptomic analysis showed that Hif1α signaling was linked to NOX4 expression, whereas no such association was seen between Hif1α and Piezo1 expression, suggesting that Hif1α was not involved in upregulation of Piezo1 by transcription. Nevertheless, it is possible that hypoxia amplifies NOX4 expression directly through Hif1α, in addition to activation by Piezo1-induced calcium Ca^{2+} influx, and thereby augments the bactericidal activity of TM PMNs.

In conclusion, the present studies show that Piezo1 is the essential mechanosensor mediating PMN activation during PMN passage through restrictive AJs into the infected tissue. Piezo1 activation in PMNs is a key host-defense adaptation mechanism required for bacterial killing in tissue through the expression of NOX4. These findings raise the possibility of cell-based therapy through adoptively transferring PMNs subjected to Piezo1 activation as a means of normalizing PMN host-defense function and preventing bacterial-induced tissue injury in diseases such as ARDS.

Limitations of the study

Although our study provides evidence for Piezo1-Hif1α-NOX4 axis-mediated mechanical signal relay in TM PMNs, the RNA-seq data also suggest involvement of other pathways and effectors as players in the mechano-transduction circuit. Future efforts in data mining from our open-source raw datasets (see STAR Methods and supplemental information for details) would expand the understanding of other mechano-transduction signaling pathways. Furthermore, the details of the mechanisms of real-time mechanical signal sensing, relay to the immediate early mediators, and specificities of mechanisms of mechano-chemical coupling are not well understood.

STAR★METHODS

Detailed methods are provided in the online version of this paper and include the following:

- KEY RESOURCES TABLE
- RESOURCE AVAILABILITY
  - Lead contact
  - Materials Availability
  - Data and code availability
- EXPERIMENTAL MODEL AND SUBJECT DETAILS
  - Human blood samples
  - Human cell lines
  - Mouse models
- METHOD DETAILS
  - Isolation of transmigrated and non-transmigrated PMN
  - Fluorescence-activated cell sorting (FACS) and flow cytometry
  - Bacterial culture
  - Phagocytosis and intracellular bacterial killing *in vitro*
  - Colocalization of Nox4 with phagosomal and phagolysosomal markers
  - Manipulation of restrictiveness of endothelial junction *in vivo*
  - Fabrication of microfluidic device
  - Chemotactic PMN transmigration through transwell pores
  - PMN isolation from bone marrow
  - Adoptive transfer
  - Clearance of lung infection

(E) NOX4 protein expression is upregulated in control but not in Piezo1-depleted HL-60-derived PMNs at 2 h post-transmigration through the Transwell system with 5-μm-diameter pore. NOX4 was not upregulated in fMLP-exposed PMNs grown in suspension or in non-transmigrated PMNs. Data are obtained from 3 independent experiments.

(F and G) Pharmacological inhibition (F) or genetic ablation (G) of NOX4 function in bone marrow and HL-60-derived PMNs, respectively, reversed the augmented bacterial killing responses induced by PMN transmigration. Data are obtained from 3 independent experiments.

(H and I) Bacterial clearance was abrogated in lungs of *Nox4*$^{\Delta PMN}$ mice. Results show *Pseudomonas aeruginosa* colonies in lungs of *Nox4*$^{fl/fl}$ and *Nox4*$^{\Delta PMN}$ mice challenged with 10^6 CFU *Pseudomonas aeruginosa* per mouse for 16 h. Lung tissue was lysed and plated on agar plates, and images of *Pseudomonas aeruginosa* colonies (H) and quantification (I) are shown. Data were obtained from 3 mice from 3 independent experiments. Scale bars, 25 mm.

(J) Piezo1 and downstream expression of NOX4 are required for ROS generation in transmigrated PMNs. ROS production measured in HL-60-derived PMNs stably transduced with control, Piezo1, or NOX4 shRNA lentiviral particles. ROS concentration was assessed at 1.5 h post-PMN transmigration through the microfluidic system. Data are obtained from 3 independent experiments. Additional information is provided as Figure S6.

- Immuno-histochemistry
- Assessment of Acute Lung Injury (ALI) Score
- Immunofluorescent staining
- Cell culture and lentiviral transgenesis
- *In vivo* lung intravital imaging of transmigrated neutrophils
- Lung intravital calcium imaging during PMN transendothelial migration
- Cremaster muscle Intravital calcium imaging during PMN transendothelial migration
- Imaging calcium in PMNs migrating through microfluidic pores
- Computational modeling and 3D simulation
- Calculating activation probability of Piezo1 channel
- Mouse survival experiments
- RNA isolation
- RT-qPCR
- RNA sequencing
- RNAseq analysis of transmigrated and non-transmigrated neutrophils

- QUANTIFICATION, STATISTICAL ANALYSIS AND REPRODUCIBILITY OF EXPERIMENTS

SUPPLEMENTAL INFORMATION

Supplemental information can be found online at https://doi.org/10.1016/j.immuni.2023.11.007.

ACKNOWLEDGMENTS

We thank Dr. Matthias Gunzer from University Duisburg-Essen, Essen, Germany for providing the Catchup mouse; Dr. Dietmar Vestweber from Max Plank Institute, Germany, for VE-PTP-VE-cadherin transgenic mouse; Qiyue Luan from University of Illinois, Chicago, for assistance with live-cell imaging; Drs. Sreeparna Chakraborty, Abhalaxmi Singh, and Abdul S. Qadir from University of Illinois, Chicago, for help with isolation of lung PMNs; Flow Cytometry Core facility for sorting and flow analysis; Research Histology Core facility for preparing H&E sections; Research Informatics Core facility for RNA-seq data analysis; Genomics Facility of University of Chicago for RNA-sequencing; and Guilan Liu and Dr. Shuangping Zhao for experiments with mice. We like to thank NIH (R01 HL045638, P01 HL 151327, P01 HL 060678, and R01 HL149300) and University of Illinois CCTS (UL1TR002003) for funding to support the work.

AUTHOR CONTRIBUTIONS

A.M.: study conceptualization, study design, experimental work, data interpretation and writing. Y.T.: intravital imaging. J.P.L.: derivation of genetic mouse models, experimental work. M.L.K.: mouse survival studies and lung infection related work made in BSL2 by W.C.C.: immunohistochemistry of lung tissues and PMN, image analyses. V.N.: providing *Nox4*$^{fl/fl}$ mice, manuscript review and editing; Z.P.: computational modeling and simulation studies. J.Z. and I.P.: design, construction, and imaging through microfluidic devices. M.M.-C.: RNA-seq data and bioinformatic analysis. C.T.: funding acquisition, manuscript review and editing; J.R.: funding acquisition, bioinformatic data analysis, manuscript review; A.B.M. and Y.K.: funding acquisition, study conceptualization, study design, manuscript writing, supervision.

DECLARATION OF INTERESTS

The authors declare no competing interests.

INCLUSION AND DIVERSITY

We support inclusive, diverse, and equitable conduct of research.

Received: March 14, 2023
Revised: August 2, 2023
Accepted: November 10, 2023
Published: December 12, 2023

REFERENCES

1. Degrossoli, A., Müller, A., Xie, K., Schneider, J.F., Bader, V., Winklhofer, K.F., Meyer, A.J., and Leichert, L.I. (2018). Neutrophil-generated HOCl leads to non-specific thiol oxidation in phagocytized bacteria. eLife *7*, e32288.
2. Dziarski, R., Platt, K.A., Gelius, E., Steiner, H., and Gupta, D. (2003). Defect in neutrophil killing and increased susceptibility to infection with nonpathogenic gram-positive bacteria in peptidoglycan recognition protein-S (PGRP-S)-deficient mice. Blood *102*, 689–697.
3. Balamayooran, G., Batra, S., Fessler, M.B., Happel, K.I., and Jeyaseelan, S. (2010). Mechanisms of neutrophil accumulation in the lungs against bacteria. Am. J. Respir. Cell Mol. Biol. *43*, 5–16.
4. Yipp, B.G., Kim, J.H., Lima, R., Zbytnuik, L.D., Petri, B., Swanlund, N., Ho, M., Szeto, V.G., Tak, T., Koenderman, L., et al. (2017). The lung is a host defense niche for immediate neutrophil-mediated vascular protection. Sci. Immunol. *2*.
5. Sekheri, M., El Kebir, D., Edner, N., and Filep, J.G. (2020). 15-Epi-LXA4 and 17-epi-RvD1 restore TLR9-mediated impaired neutrophil phagocytosis and accelerate resolution of lung inflammation. Proc. Natl. Acad. Sci. USA *117*, 7971–7980.
6. Nourshargh, S., and Alon, R. (2014). Leukocyte migration into inflamed tissues. Immunity *41*, 694–707.
7. Mittal, M., Nepal, S., Tsukasaki, Y., Hecquet, C.M., Soni, D., Rehman, J., Tiruppathi, C., and Malik, A.B. (2017). Neutrophil activation of endothelial cell-expressed TRPM2 mediates transendothelial neutrophil migration and vascular injury. Circ. Res. *121*, 1081–1091.
8. Prinyakupt, J., and Pluempitiwiriyawej, C. (2015). Segmentation of white blood cells and comparison of cell morphology by linear and naive Bayes classifiers. Biomed. Eng. OnLine *14*, 63.
9. Etich, J., Bergmeier, V., Frie, C., Kreft, S., Bengestrate, L., Eming, S., Mauch, C., Eckes, B., Ulus, H., Lund, F.E., et al. (2013). PECAM1(+)/Sca1(+)/CD38(+) vascular cells transform into myofibroblast-like cells in skin wound repair. PLoS One *8*, e53262.
10. Niemiec, M.J., De Samber, B., Garrevoet, J., Vergucht, E., Vekemans, B., De Rycke, R., Björn, E., Sandblad, L., Wellenreuther, G., Falkenberg, G., et al. (2015). Trace element landscape of resting and activated human neutrophils on the sub-micrometer level. Metallomics *7*, 996–1010.
11. Grinstein, S., Furuya, W., and Cragoe, E.J., Jr. (1986). Volume changes in activated human neutrophils: the role of Na+/H+ exchange. J. Cell. Physiol. *128*, 33–40.
12. Muller, W.A. (2011). Mechanisms of leukocyte transendothelial migration. Annu. Rev. Pathol. *6*, 323–344.
13. Heemskerk, N., Schimmel, L., Oort, C., van Rijssel, J., Yin, T., Ma, B., van Unen, J., Pitter, B., Huveneers, S., Goedhart, J., et al. (2016). F-actin-rich contractile endothelial pores prevent vascular leakage during leukocyte diapedesis through local RhoA signalling. Nat. Commun. *7*, 10493.
14. Hind, L.E., Ingram, P.N., Beebe, D.J., and Huttenlocher, A. (2018). Interaction with an endothelial lumen increases neutrophil lifetime and motility in response to P aeruginosa. Blood *132*, 1818–1828.
15. Grönloh, M.L.B., Arts, J.J.G., and van Buul, J.D. (2021). Neutrophil transendothelial migration hotspots - mechanisms and implications. J. Cell Sci. *134*, jcs255653.
16. Stroka, K.M., and Aranda-Espinoza, H. (2011). Endothelial cell substrate stiffness influences neutrophil transmigration via myosin light chain kinase-dependent cell contraction. Blood *118*, 1632–1640.
17. Warnatsch, A., Tsourouktsoglou, T.D., Branzk, N., Wang, Q., Reincke, S., Herbst, S., Gutierrez, M., and Papayannopoulos, V. (2017). Reactive oxygen species localization programs inflammation to clear microbes of different size. Immunity *46*, 421–432.

18. Lee, W.L., Harrison, R.E., and Grinstein, S. (2003). Phagocytosis by neutrophils. Microbes Infect. *5*, 1299–1306.

19. Dale, D.C., Boxer, L., and Liles, W.C. (2008). The phagocytes: neutrophils and monocytes. Blood *112*, 935–945.

20. Panday, A., Sahoo, M.K., Osorio, D., and Batra, S. (2015). NADPH oxidases: an overview from structure to innate immunity-associated pathologies. Cell. Mol. Immunol. *12*, 5–23.

21. O'Neill, S., Brault, J., Stasia, M.J., and Knaus, U.G. (2015). Genetic disorders coupled to ROS deficiency. Redox Biol. *6*, 135–156.

22. Deffert, C., Cachat, J., and Krause, K.H. (2014). Phagocyte NADPH oxidase, chronic granulomatous disease and mycobacterial infections. Cell. Microbiol. *16*, 1168–1178.

23. Buvelot, H., Posfay-Barbe, K.M., Linder, P., Schrenzel, J., and Krause, K.H. (2017). Staphylococcus aureus, phagocyte NADPH oxidase and chronic granulomatous disease. FEMS Microbiol. Rev. *41*, 139–157.

24. Canton, J., and Grinstein, S. (2014). Priming and activation of NADPH oxidases in plants and animals. Trends Immunol. *35*, 405–407.

25. Fairn, G.D., and Grinstein, S. (2012). How nascent phagosomes mature to become phagolysosomes. Trends Immunol. *33*, 397–405.

26. Moltyaner, Y., Geerts, W.H., Chamberlain, D.W., Heyworth, P.G., Noack, D., Rae, J., Doyle, J.J., and Downey, G.P. (2003). Underlying chronic granulomatous disease in a patient with bronchocentric granulomatosis. Thorax *58*, 1096–1098.

27. Winterbourn, C.C., Kettle, A.J., and Hampton, M.B. (2016). Reactive oxygen species and neutrophil function. Annu. Rev. Biochem. *85*, 765–792.

28. Coste, B., Mathur, J., Schmidt, M., Earley, T.J., Ranade, S., Petrus, M.J., Dubin, A.E., and Patapoutian, A. (2010). Piezo1 and Piezo2 are essential components of distinct mechanically activated cation channels. Science *330*, 55–60.

29. Kefauver, J.M., Ward, A.B., and Patapoutian, A. (2020). Discoveries in structure and physiology of mechanically activated ion channels. Nature *587*, 567–576.

30. Nisimoto, Y., Diebold, B.A., Cosentino-Gomes, D., and Lambeth, J.D. (2014). Nox4: a hydrogen peroxide-generating oxygen sensor. Biochemistry *53*, 5111–5120.

31. Buck, T., Hack, C.T., Berg, D., Berg, U., Kunz, L., and Mayerhofer, A. (2019). The NADPH oxidase 4 is a major source of hydrogen peroxide in human granulosa-lutein and granulosa tumor cells. Sci. Rep. *9*, 3585.

32. von Löhneysen, K., Noack, D., Wood, M.R., Friedman, J.S., and Knaus, U.G. (2010). Structural insights into Nox4 and Nox2: motifs involved in function and cellular localization. Mol. Cell. Biol. *30*, 961–975.

33. Yap, B., and Kamm, R.D. (2005). Mechanical deformation of neutrophils into narrow channels induces pseudopod projection and changes in biomechanical properties. J. Appl. Physiol. (1985) *98*, 1930–1939.

34. Makino, A., Shin, H.Y., Komai, Y., Fukuda, S., Coughlin, M., Sugihara-Seki, M., and Schmid-Schönbein, G.W. (2007). Mechanotransduction in leukocyte activation: a review. Biorheology *44*, 221–249.

35. Kumar, S. (2014). Stiffness does matter. Nat. Mater. *13*, 918–920.

36. Chiang, E.Y., Hidalgo, A., Chang, J., and Frenette, P.S. (2007). Imaging receptor microdomains on leukocyte subsets in live mice. Nat. Methods *4*, 219–222.

37. Hasenberg, A., Hasenberg, M., Männ, L., Neumann, F., Borkenstein, L., Stecher, M., Kraus, A., Engel, D.R., Klingberg, A., Seddigh, P., et al. (2015). Catchup: a mouse model for imaging-based tracking and modulation of neutrophil granulocytes. Nat. Methods *12*, 445–452.

38. Broermann, A., Winderlich, M., Block, H., Frye, M., Rossaint, J., Zarbock, A., Cagna, G., Linnepe, R., Schulte, D., Nottebaum, A.F., et al. (2011). Dissociation of VE-PTP from VE-cadherin is required for leukocyte extravasation and for VEGF-induced vascular permeability in vivo. J. Exp. Med. *208*, 2393–2401.

39. Friedrich, E.E., Hong, Z., Xiong, S., Zhong, M., Di, A., Rehman, J., Komarova, Y.A., and Malik, A.B. (2019). Endothelial cell Piezo1 mediates pressure-induced lung vascular hyperpermeability via disruption of adherens junctions. Proc. Natl. Acad. Sci. USA *116*, 12980–12985.

40. Nawroth, R., Poell, G., Ranft, A., Kloep, S., Samulowitz, U., Fachinger, G., Golding, M., Shima, D.T., Deutsch, U., and Vestweber, D. (2002). VE-PTP and VE-cadherin ectodomains interact to facilitate regulation of phosphorylation and cell contacts. EMBO J. *21*, 4885–4895.

41. Gotsch, U., Borges, E., Bosse, R., Böggemeyer, E., Simon, M., Mossmann, H., and Vestweber, D. (1997). VE-cadherin antibody accelerates neutrophil recruitment in vivo. J. Cell Sci. *110*, 583–588.

42. Suresh Kumar, V., Sadikot, R.T., Purcell, J.E., Malik, A.B., and Liu, Y. (2014). Pseudomonas aeruginosa induced lung injury model. J. Vis. Exp. e52044.

43. Murthy, S.E., Dubin, A.E., and Patapoutian, A. (2017). Piezos thrive under pressure: mechanically activated ion channels in health and disease. Nat. Rev. Mol. Cell Biol. *18*, 771–783.

44. Millius, A., and Weiner, O.D. (2010). Manipulation of neutrophil-like HL-60 cells for the study of directed cell migration. Methods Mol. Biol. *591*, 147–158.

45. Thastrup, O., Cullen, P.J., Drøbak, B.K., Hanley, M.R., and Dawson, A.P. (1990). Thapsigargin, a tumor promoter, discharges intracellular Ca2+ stores by specific inhibition of the endoplasmic reticulum Ca2(+)-ATPase. Proc. Natl. Acad. Sci. USA *87*, 2466–2470.

46. Liu, C., and Hermann, T.E. (1978). Characterization of ionomycin as a calcium ionophore. J. Biol. Chem. *253*, 5892–5894.

47. Lin, Y.C., Guo, Y.R., Miyagi, A., Levring, J., MacKinnon, R., and Scheuring, S. (2019). Force-induced conformational changes in PIEZO1. Nature *573*, 230–234.

48. Peng, Z., Pak, O.S., Feng, Z., Liu, A.P., and Young, Y.-N. (2016). On the gating of mechanosensitive channels by fluid shear stress. Acta Mech. Sin. *32*, 1012–1022.

49. Ranade, S.S., Qiu, Z., Woo, S.H., Hur, S.S., Murthy, S.E., Cahalan, S.M., Xu, J., Mathur, J., Bandell, M., Coste, B., et al. (2014). Piezo1, a mechanically activated ion channel, is required for vascular development in mice. Proc. Natl. Acad. Sci. USA *111*, 10347–10352.

50. Syeda, R., Xu, J., Dubin, A.E., Coste, B., Mathur, J., Huynh, T., Matzen, J., Lao, J., Tully, D.C., Engels, I.H., et al. (2015). Chemical activation of the mechanotransduction channel Piezo1. eLife *4*, e07369.

51. Solis, A.G., Bielecki, P., Steach, H.R., Sharma, L., Harman, C.C.D., Yun, S., de Zoete, M.R., Warnock, J.N., To, S.D.F., York, A.G., et al. (2019). Mechanosensation of cyclical force by PIEZO1 is essential for innate immunity. Nature *573*, 69–74.

52. Yamada, M., Kubo, H., Kobayashi, S., Ishizawa, K., He, M., Suzuki, T., Fujino, N., Kunishima, H., Hatta, M., Nishimaki, K., et al. (2011). The increase in surface CXCR4 expression on lung extravascular neutrophils and its effects on neutrophils during endotoxin-induced lung injury. Cell. Mol. Immunol. *8*, 305–314.

53. Green, D.E., Murphy, T.C., Kang, B.Y., Kleinhenz, J.M., Szyndralewiez, C., Page, P., Sutliff, R.L., and Hart, C.M. (2012). The Nox4 inhibitor GKT137831 attenuates hypoxia-induced pulmonary vascular cell proliferation. Am. J. Respir. Cell Mol. Biol. *47*, 718–726.

54. Artemenko, Y., Axiotakis, L., Jr., Borleis, J., Iglesias, P.A., and Devreotes, P.N. (2016). Chemical and mechanical stimuli act on common signal transduction and cytoskeletal networks. Proc. Natl. Acad. Sci. USA *113*, E7500–E7509.

55. Ekpenyong, A.E., Toepfner, N., Chilvers, E.R., and Guck, J. (2015). Mechanotransduction in neutrophil activation and deactivation. Biochim. Biophys. Acta *1853*, 3105–3116.

56. Burns, A.R., Smith, C.W., and Walker, D.C. (2003). Unique structural features that influence neutrophil emigration into the lung. Physiol. Rev. *83*, 309–336.

57. Nauseef, W.M., and Borregaard, N. (2014). Neutrophils at work. Nat. Immunol. *15*, 602–611.

58. Komarova, Y.A., Kruse, K., Mehta, D., and Malik, A.B. (2017). Protein interactions at endothelial junctions and signaling mechanisms regulating endothelial permeability. Circ. Res. *120*, 179–206.

59. Juettner, V.V., Kruse, K., Dan, A., Vu, V.H., Khan, Y., Le, J., Leckband, D., Komarova, Y., and Malik, A.B. (2019). VE-PTP stabilizes VE-cadherin

junctions and the endothelial barrier via a phosphatase-independent mechanism. J. Cell Biol. *218*, 1725–1742.

60. Tsuda, Y., Takahashi, H., Kobayashi, M., Hanafusa, T., Herndon, D.N., and Suzuki, F. (2004). Three different neutrophil subsets exhibited in mice with different susceptibilities to infection by methicillin-resistant Staphylococcus aureus. Immunity *21*, 215–226.
61. Schauer, C., Janko, C., Munoz, L.E., Zhao, Y., Kienhöfer, D., Frey, B., Lell, M., Manger, B., Rech, J., Naschberger, E., et al. (2014). Aggregated neutrophil extracellular traps limit inflammation by degrading cytokines and chemokines. Nat. Med. *20*, 511–517.
62. Ngamsri, K.C., Fuhr, A., Schindler, K., Simelitidis, M., Hagen, M., Zhang, Y., Gamper-Tsigaras, J., and Konrad, F.M. (2022). Sevoflurane dampens acute pulmonary inflammation via the adenosine receptor A2B and heme oxygenase-1. Cells *11*, 1094.
63. Hann, J., Bueb, J.L., Tolle, F., and Bréchard, S. (2020). Calcium signaling and regulation of neutrophil functions: still a long way to go. J. Leukoc. Biol. *107*, 285–297.
64. Vig, M., and Kinet, J.P. (2009). Calcium signaling in immune cells. Nat. Immunol. *10*, 21–27.
65. Feske, S. (2007). Calcium signalling in lymphocyte activation and disease. Nat. Rev. Immunol. *7*, 690–702.
66. Santana Nunez, D., Malik, A.B., Lee, Q., Ahn, S.J., Coctecon-Murillo, A., Lazarko, D., Levitan, I., Mehta, D., and Komarova, Y.A. (2023). Piezo1 induces endothelial responses to shear stress via soluble adenylyl cyclase-IP(3)R2 circuit. iScience *26*, 106661.
67. Hoffmann, K., Sperling, K., Olins, A.L., and Olins, D.E. (2007). The granulocyte nucleus and lamin B receptor: avoiding the ovoid. Chromosoma *116*, 227–235.
68. Doerschuk, C.M., Beyers, N., Coxson, H.O., Wiggs, B., and Hogg, J.C. (1993). Comparison of neutrophil and capillary diameters and their relation to neutrophil sequestration in the lung. J. Appl. Physiol. (1985) *74*, 3040–3045.
69. Shin, J.W., Spinler, K.R., Swift, J., Chasis, J.A., Mohandas, N., and Discher, D.E. (2013). Lamins regulate cell trafficking and lineage maturation of adult human hematopoietic cells. Proc. Natl. Acad. Sci. USA *110*, 18892–18897.
70. Diebold, I., Petry, A., Hess, J., and Görlach, A. (2010). The NADPH oxidase subunit NOX4 is a new target gene of the hypoxia-inducible factor-1. Mol. Biol. Cell *21*, 2087–2096.
71. Liu, Y.V., Hubbi, M.E., Pan, F., McDonald, K.R., Mansharamani, M., Cole, R.N., Liu, J.O., and Semenza, G.L. (2007). Calcineurin promotes hypoxia-inducible factor 1alpha expression by dephosphorylating RACK1 and blocking RACK1 dimerization. J. Biol. Chem. *282*, 37064–37073.
72. Davey, M.E., Caiazza, N.C., and O'Toole, G.A. (2003). Rhamnolipid surfactant production affects biofilm architecture in Pseudomonas aeruginosa PAO1. J. Bacteriol. *185*, 1027–1036.
73. Kuroda, J., Ago, T., Matsushima, S., Zhai, P., Schneider, M.D., and Sadoshima, J. (2010). NADPH oxidase 4 (Nox4) is a major source of oxidative stress in the failing heart. Proc. Natl. Acad. Sci. USA *107*, 15565–15570.
74. Gille, C., Spring, B., Tewes, L., Poets, C.F., and Orlikowsky, T. (2006). A new method to quantify phagocytosis and intracellular degradation using green fluorescent protein-labeled Escherichia coli: comparison of cord blood macrophages and peripheral blood macrophages of healthy adults. Cytometry A *69*, 152–154.
75. Isberg, R.R., and Falkow, S. (1985). A single genetic locus encoded by Yersinia pseudotuberculosis permits invasion of cultured animal cells by Escherichia coli K-12. Nature *317*, 262–264.
76. Chow, C.W., Downey, G.P., and Grinstein, S. (2004). Measurements of phagocytosis and phagosomal maturation. Curr. Protoc. Cell Biol. *Chapter 15*. Unit 15.7.
77. Bolte, S., and Cordelières, F.P. (2006). A guided tour into subcellular colocalization analysis in light microscopy. J. Microsc. *224*, 213–232.
78. Mukherjee, P., Nebuloni, F., Gao, H., Zhou, J., and Papautsky, I. (2019). Rapid prototyping of soft lithography masters for microfluidic devices using dry film photoresist in a non-cleanroom setting. Micromachines (Basel) *10*, 192.
79. Shelly, M., Lee, S.I., Suarato, G., Meng, Y., and Pautot, S. (2017). Photolithography-based substrate microfabrication for patterning semaphorin 3A to study neuronal development. Methods Mol. Biol. *1493*, 321–343.
80. Matute-Bello, G., Downey, G., Moore, B.B., Groshong, S.D., Matthay, M.A., Slutsky, A.S., and Kuebler, W.M.; Acute Lung Injury in Animals Study Group (2011). An official American Thoracic Society workshop report: features and measurements of experimental acute lung injury in animals. Am. J. Respir. Cell Mol. Biol. *44*, 725–738.
81. Looney, M.R., Thornton, E.E., Sen, D., Lamm, W.J., Glenny, R.W., and Krummel, M.F. (2011). Stabilized imaging of immune surveillance in the mouse lung. Nat. Methods *8*, 91–96.
82. Tsukasaki, Y., Toth, P.T., Davoodi-Bojd, E., Rehman, J., and Malik, A.B. (2022). Quantitative pulmonary neutrophil dynamics using computer-vision stabilized intravital imaging. Am. J. Respir. Cell Mol. Biol. *66*, 12–22.
83. Li, J., Kim, K., Hahm, E., Molokie, R., Hay, N., Gordeuk, V.R., Du, X., and Cho, J. (2014). Neutrophil AKT2 regulates heterotypic cell-cell interactions during vascular inflammation. J. Clin. Invest. *124*, 1483–1496.
84. Liu, L., Cara, D.C., Kaur, J., Raharjo, E., Mullaly, S.C., Jongstra-Bilen, J., Jongstra, J., and Kubes, P. (2005). LSP1 is an endothelial gatekeeper of leukocyte transendothelial migration. J. Exp. Med. *201*, 409–418.
85. Lu, H., and Peng, Z. (2019). Boundary integral simulations of a red blood cell squeezing through a submicron slit under prescribed inlet and outlet pressures. Phys. Fluids *31*, 31902.
86. Evans, E., and Yeung, A. (1989). Apparent viscosity and cortical tension of blood granulocytes determined by micropipet aspiration. Biophys. J. *56*, 151–160.
87. Tsai, M.A., Frank, R.S., and Waugh, R.E. (1993). Passive mechanical behavior of human neutrophils: power-law fluid. Biophys. J. *65*, 2078–2088.
88. Lewis, A.H., and Grandl, J. (2015). Mechanical sensitivity of Piezo1 ion channels can be tuned by cellular membrane tension. eLife *4*, e12088.
89. Cox, C.D., Bae, C., Ziegler, L., Hartley, S., Nikolova-Krstevski, V., Rohde, P.R., Ng, C.A., Sachs, F., Gottlieb, P.A., and Martinac, B. (2016). Removal of the mechanoprotective influence of the cytoskeleton reveals PIEZO1 is gated by bilayer tension. Nat. Commun. *7*, 10366.
90. Yang, X., Lin, C., Chen, X., Li, S., Li, X., and Xiao, B. (2022). Structure deformation and curvature sensing of PIEZO1 in lipid membranes. Nature *604*, 377–383.
91. Schmittgen, T.D., and Livak, K.J. (2008). Analyzing real-time PCR data by the comparative C(T) method. Nat. Protoc. *3*, 1101–1108.
92. Dobin, A., Davis, C.A., Schlesinger, F., Drenkow, J., Zaleski, C., Jha, S., Batut, P., Chaisson, M., and Gingeras, T.R. (2013). STAR: ultrafast universal RNA-seq aligner. Bioinformatics *29*, 15–21.
93. Liao, Y., Smyth, G.K., and Shi, W. (2014). featureCounts: an efficient general purpose program for assigning sequence reads to genomic features. Bioinformatics *30*, 923–930.
94. McCarthy, D.J., Chen, Y., and Smyth, G.K. (2012). Differential expression analysis of multifactor RNA-Seq experiments with respect to biological variation. Nucleic Acids Res. *40*, 4288–4297.
95. Robinson, M.D., McCarthy, D.J., and Smyth, G.K. (2010). edgeR: a Bioconductor package for differential expression analysis of digital gene expression data. Bioinformatics *26*, 139–140.
96. Benjamini, Y., and Hochberg, Y. (1995). Controlling the false discovery rate: a practical and powerful approach to multiple testing. J. R. Stat. Soc. Ser. B Methodol. *57*, 289–300.
97. Geyer, M., Huang, F., Sun, Y., Vogel, S.M., Malik, A.B., Taylor, C.W., and Komarova, Y.A. (2015). Microtubule-associated protein EB3 regulates IP3 receptor clustering and Ca(2+) signaling in endothelial cells. Cell Rep. *12*, 79–89.

Please cite this article in press as: Mukhopadhyay et al., *trans*-Endothelial neutrophil migration activates bactericidal function via Piezo1 mechanosensing, Immunity (2023), https://doi.org/10.1016/j.immuni.2023.11.007

STAR★METHODS

KEY RESOURCES TABLE

REAGENT or RESOURCE	SOURCE	IDENTIFIER
Antibodies		
Rat monoclonal α-mouse Ly-6G conjugated with Brilliant Violet 421™	Biolegend	RRID: AB_2562567; Cat #127628
Rat monoclonal α-mouse Ly-6G conjugated with Alexa Fluor® 594	Biolegend	RRID: AB_2563207; Cat #127636
Rat monoclonal α-VE-cadherin	BD Biosciences	Cat #555289
Rat monoclonal isotype control	BD Biosciences	Cat # 559073
Mouse monoclonal α-Green fluorescent protein	Santa Cruz Biotechnology	Cat # sc-9996
Rabbit polyclonal α-CD31 (PECAM1)	Abcam	Cat # ab28364
Rat monoclonal α-mouse CD31 conjugated with Brilliant Violet 421™	Biolegend	RRID: AB_2650892; Cat # 102424
Rabbit polyclonal α-Piezo1	Proteintech	Cat # 15939-1-AP
Rabbit polyclonal α-Nox4	Novus	Cat # NB110-58849
Rabbit polyclonal α-Vinculin	Abcam	Cat # ab129002
Mouse monoclonal α-LAMP1 (D4O1S)	Cell Signaling	Cat # 15665
Rabbit monoclonal α-RAB7 (D95F2)	Cell Signaling	Cat # 9367
Syrian hamster monoclonal α-Podoplanin (PDPN)	DSHB	Cat # 8.1.1
Rabbit polyclonal α-RAB5A	Proteintech	Cat # 11947-1-AP
APC anti-human CD62L Antibody	Biolegend	RRID: AB_314469; Cat # 304809
Brilliant Violet 510™ anti-human CD184 (CXCR4) Antibody	Biolegend	RRID: AB_2810460; Cat # 306535
Brilliant Violet 711™ anti-human CD15 (SSEA-1) Antibody	Biolegend	RRID: AB_2750191; Cat # 323049
Alexa Fluor® 700 anti-human CD47 Antibody	Biolegend	RRID: AB_2716204; Cat # 323125
Brilliant Violet 785™ anti-human CD10 Antibody	Biolegend	RRID: AB_2860829; Cat # 312237
Brilliant Violet 650™ anti-human CD15 (SSEA-1) Antibody	Biolegend	RRID: AB_2562499; Cat # 323033
Alexa Fluor® 594 anti-mouse/human CD11b Antibody	Biolegend	RRID: AB_2563231; Cat # 101254
Zombie NIR live dead stain	Biolegend	Cat # 77184
Bacterial and virus strains		
Escherichia coli -GFP	ATCC	Cat #25922GFP
Pseudomonas aeruginosa (PA-GFP-01 strain)	Laboratory of Terry Manchen	Davey et al.[72]
Chemicals, peptides, and recombinant proteins		
The collagenase type I from *Clostridium histolyticum*	Millipore-Sigma	Cat # SCR103
Lipopolysaccharides from *Escherichia coli* O55:B5	Millipore-Sigma	Cat # L2880
Carbenicillin	Goldbio	Cat #C-103-5
Everolimus	Millipore-Sigma	Cat # SML2282
Formaldehyde solution	Millipore-Sigma	Cat # HT501128
N-Formyl-Met-Leu-Phe	Millipore-Sigma	Cat # F3506
Puromycin	Millipore-Sigma	Cat # P8833
Fluor-4, AM	Invitrogen	Cat # F14201
CellMask™ Deep Red Plasma membrane stain	Thermo Fisher	Cat #C10046
E. coli-derived mouse CXCL2/GRO beta/MIP-2/CINC-3 protein	R&D Systems	Cat # 452-M2-050
Yoda1	Millipore-Sigma	Cat # SML1558
Setanaxib (GKT137831)	Selleckchem	Cat # S7171
Thapsigargin	Millipore-Sigma	Cat # T9033
Ionomycin	Millipore-Sigma	Cat # I9657

(*Continued on next page*)

Please cite this article in press as: Mukhopadhyay et al., *trans*-Endothelial neutrophil migration activates bactericidal function via Piezo1 mechanosensing, Immunity (2023), https://doi.org/10.1016/j.immuni.2023.11.007

Continued

REAGENT or RESOURCE	SOURCE	IDENTIFIER
Amplex red reagent	Invitrogen	Cat # A22188
FastStart Universal SYBR Green Master	Millipore-Sigma	Cat # 4913914001
Pico Plus	Thermo Fischer	Cat # 34580
Critical commercial assays		
High-capacity cDNA reverse transcription kit"	Thermo Fisher	Cat #4368814
RNeasy Plus kit	Qiagen	Cat # #74034
Easystep human neutrophil isolation kit	Stemcell technologies	Cat #19666
Pierce BCA Protein Assay Kit	Thermo Fischer	Cat # 23225
neutrophil elastase ELISA kit	Abcam	Cat # ab252356
Experimental models: Cell lines		
Human promyelocytic leukemia (HL-60) cells	ATCC	Cat # CCL-240
C57BL/6 Mouse Primary Lung Microvascular Endothelial Cells	Cell Biologics	Cat # C57-6011
Experimental models: Organisms/strains		
Mouse: C57BL/6	The Jackson Laboratory	RRID: IMSR_JAX:000664
Mouse: C57BL/6-Ly6g(tm2621(Cre-tdTomato)	from Dr. Matthias Gunzer's lab	Hasenberg et al.[37]
Mouse: $Cdh5^{tm4(Cdh5/Fkbp,Ptprb/Mtor*)Dvst}$	from Dr. Dietmar Vestweber's lab	Broermann et al.[38]
Mouse: B6.Cg-Piezo1tm2.1Apat/J	The Jackson Laboratory	RRID: #IMSR_JAX:029213
Mouse: B6(129S4)-*Gt(ROSA)26Sor*$^{tm1.1(CAG-tdTomato/GCaMP6f)Mdcah}$/J	The Jackson Laboratory	RRID: #IMSR_JAX:031968
Mouse: Nox4 floxed	from Dr. Junichi Sadoshima	Kuroda et al.[73]
$Piezo1^{\Delta PMN}$	this manuscript	N/A
$NOX4^{\Delta PMN}$	this manuscript	N/A
Oligonucleotides		
MISSION® shRNA lentiviral particles Piezo1 shRNA#2: CTCACCAAGAAGTACAATCAT	Millipore-Sigma	TRCN0000121969
MISSION® shRNA lentiviral particles Piezo1 shRNA#3: GTACTTCGTGAAGTGCATCTA	Millipore-Sigma	TRCN0000143190
MISSION® shRNA lentiviral particles Nox4 shRNA#1: GAGCCTCAGCATCTGTTCTTA	Millipore-Sigma	TRCN0000046092
MISSION® shRNA lentiviral particles Nox4 shRNA#2: CAGAGTTTACCCAGCACAAAT	Millipore-Sigma	TRCN0000046091
MISSION® shRNA lentiviral particles Nox4 shRNA#3: CCCTCAACTTCTCAGTGAATT	Millipore-Sigma	TRCN0000046090
MISSION® shRNA lentiviral particles Nox4 shRNA#4: GCTGTATATTGATGGTCCTTT	Millipore-Sigma	TRCN0000046089
MISSION® shRNA lentiviral particles Nox4 shRNA#5: CCTGTGGTGTTACTATCTGTA	Millipore-Sigma	TRCN0000046088
MISSION® shRNA lentiviral particles Hif1α shRNA#1: CCGCTGGAGACACAATCATAT	Millipore-Sigma	TRCN0000003808
MISSION® shRNA lentiviral particles Hif1α shRNA#2: CCAGTTATGATTGTGAAGTTA	Millipore-Sigma	TRCN0000003809
MISSION® shRNA lentiviral particles Hif1α shRNA#3: GTGATGAAAGAATTACCGAAT	Millipore-Sigma	TRCN0000003810
MISSION® shRNA lentiviral particles Hif1α shRNA#4: CGGCGAAGTAAAGAATCTGAA	Millipore-Sigma	TRCN0000003811
MISSION® shRNA lentiviral particles Hif1α shRNA#5: TGCTCTTTGTGGTTGGATCTA	Millipore-Sigma	TRCN0000010819
Primer: Nox1 Forward: CCGGTCATTCTTTATATCTGTG	This manuscript	N/A

(*Continued on next page*)

Continued

REAGENT or RESOURCE	SOURCE	IDENTIFIER
Primer: Nox1 Reserved: CAACCTTGGTAATCACAACC	This manuscript	N/A
Primer: Nox3 Forward: CAAACACAACCACTGAATTG	This manuscript	N/A
Primer: Nox3 Reserved: CATGATCAAGACTAAAGCCAG	This manuscript	N/A
Primer: Nox4 Forward: AGTCCTTCCGTTGGTTTG	This manuscript	N/A
Primer: Nox4 Reserved: AAAGTTTCCACCGAGGAC	This manuscript	N/A
Primer: Nox5 Forward: AGGTGTTCTATTGGACTCAC	This manuscript	N/A
Primer: Nox5 Reserved: CTCCAGGAAAAACAAGATTCC	This manuscript	N/A
Primers: Nox2	Santa Cruz Biotechnology	Cat # 35503-PR
Software and algorithms		
SUMMIT, 6.1	Beckman Coulter	https://www.beckmancoulter.com/wsrportal/techdocs?docname=cyan_adp_instructions_for_use.pdf
Kaluza Analysis 2.1	Beckman Coulter	https://www.beckman.com/flow-cytometry/software/kaluza
E. coli calculator	Agilent	https://www.agilent.com/store/biocalculators/calcODBacterial.jsp
AutoCAD	AutoDESK	https://www.autodesk.com/products/autocad/overview?term=1-YEAR&tab=subscription
Countess™ 3	Thermo Fisher	https://www.thermofisher.com/order/catalog/product/A51025
Rspace	Netzsch	https://analyzing-testing.netzsch.com/en-US/products/software/rspace-software
Aperio ImageScope	Leica Biosystems	https://www.leicabiosystems.com/us/digital-pathology/manage/aperio-imagescope/
Zen	Carl Zeiss	https://www.zeiss.com/microscopy/us/products/microscope-software/zen.html
Alpha Fold	DeepMind	https://alphafold.ebi.ac.uk/
UCSF Chimera	UCSF	https://www.cgl.ucsf.edu/chimera/
Image j	NIH	https://imagej.nih.gov/ij/notes.html
Slidebook (3i)	Intelligent Imaging	https://www.intelligent-imaging.com/slidebook
In-house computer vision algorithms [8180808080802] for lung 2-photon intravital imaging	Yoshikaju Tsukasaki (Author of this paper)	(https://github.com/YoshiTsukasaki/CoVSTii or https://uofi.box.com/v/StandaloneCoVSTii)
LabView	National instruments corp.	https://www.ni.com/en-us/shop/labview.html
Paraview 5.7.0	Kitware	https://www.paraview.org/
Cellsens	Olympus	https://www.olympus-lifescience.com/en/software/cellsens/
Cutadapt v3.4	Marcel Martin	https://cutadapt.readthedocs.io/en/v3.4/installation.html
STAR v2.7.0 aligner	Alexander Dobin	https://academic.oup.com/bioinformatics/article/29/1/15/272537
FeatureCounts v1.5.0	Yang Liao	http://subread.sourceforge.net/

(*Continued on next page*)

Continued

REAGENT or RESOURCE	SOURCE	IDENTIFIER
R package edgeR v.3.36	https://www.r-project.org/	https://bioconductor.org/packages/release/bioc/html/edgeR.html
Ingenuity Pathway Analysis	Qiagen	https://digitalinsights.qiagen.com/products-overview/discovery-insights-portfolio/analysis-and-visualization/qiagen-ipa/
Gene Ontology Biological Process	MSigDB	https://www.gsea-msigdb.org/gsea/msigdb/
Origin Pro	Origin lab	https://www.originlab.com/origin
Prism	Graphpad	https://www.graphpad.com/scientific-software/prism/
Illustrator	Adobe	https://www.adobe.com/products/illustrator.html
Biorender	Biorender	https://biorender.com/
Spectroflo 2.2.1	Cytek Biosciences	https://cytekbio.com/pages/spectro-flo
Other		
RBC lysis buffer	Thermo Fisher	Cat #00-4333-57
RPMI 1640 Medium, HEPES	Thermo Fisher	Cat #22400089
Endothelial Cell Medium /w Kit	Cell Biologics	Cat # M1168
Cell strainer	Thermo Fisher	Cat #08-771-1
polyethylene terephthalate insert 3μm diam.	Millipore-Sigma	Cat #MCSP24H48
polyethylene terephthalate insert 5μm diam.	Millipore-Sigma	Cat #MCMP24H48
polyethylene terephthalate insert 8μm diam.	Millipore-Sigma	Cat #MCEP24H48
polycarbonate insert 12 μm diam.	Millipore-Sigma	Cat #PIXP01250
Percoll® PLUS	GE Healthcare	Cat #17-0891-01

RESOURCE AVAILABILITY

Lead contact

Further information and requests for resources and reagents should be directed to and will be fulfilled by the lead contact, Asrar B. Malik (abmalik@uic.edu).

Materials Availability

Requests for reagents and resources generated in this study will be fulfilled by the lead contact, Asrar B. Malik (abmalik@uic.edu).

Data and code availability

Sequencing data is available on Gene Expression Omnibus. The accession number is GSE210111. The reviewer token is wlebcwqwdncrvir. Computational modeling and simulation data is uploaded using indigo: https://figshare.com/s/0eac4b5603eff08aba58.

EXPERIMENTAL MODEL AND SUBJECT DETAILS

Human blood samples

All studies involving human subjects were performed in accordance with the Declaration of Helsinki and approved by the University of Illinois at Chicago's Institutional Review Board (IRB). Human peripheral blood was collected by venipuncture from 11 random healthy volunteers of 18 years of age or older, recruited in an unbiased fashion irrespective of ethnicity and gender. Donors provided written informed consent that was documented. Information about gender was collected. Gender-based analysis was not performed due to low number of recruited donors per experiment (3-5 donor of both genders per experiment). Blood PMNs were isolated by immune-magnetic negative selection method (Easystep human neutrophil isolation kit, Stemcell technologies, #19666). 80-100 x 10^6 PMN yield were obtained from 20 ml of human blood.

Human cell lines

Human promyelocytic leukemia (HL-60) cells (ATCC #CCL-240)[44] were grown in suspension with RPMI1640 medium containing L-glutamine and 25 mM HEPES (Thermo Fisher #72400047), supplemented with 15% FBS (Thermo Fisher #A4766801) and penicillin-streptomycin-amphotericin B (Thermo Fisher #15240096), at 37°C, 5% CO_2. Cells were passaged before the density reached 2x10^6/ml in 25 cm^2 flask. HL-60 cell were differentiated into PMN-like cells with 1.3% DMSO for 6 days. Differentiated

cells were routinely stained for DNA using 4′,6-diamidino-2-phenylindole (DAPI) or *Hoechst 33342* and appeared to be free of cytosolic DNA.

Mouse models

All the mice were handled in accordance with NIH guidelines for the care and use of laboratory animals and UIC animal care and use committee (ACC)'s regulations. All procedures were approved by the UIC IACUC. Male mice of 8-10 weeks of age, body weight ranging from 18-22 g, were used for all experiments. C57BL/6 (IMSR_JAX:000664) mice were purchased from Jackson laboratory. C57BL/6-Ly6g(tm2621(Cre-tdTomato), known as "Catchup" mice were a gift from Dr. Matthias Gunzer.[37] VE-cadherin-FKBP - VE-PTP-FRB (known as: Cdh5$^{tm4(Cdh5/Fkbp,Ptprb/Mtor*)Dvst}$) mice were a gift from Dr. Dietmar Vestweber[38]. In these mice, the two coding sequences of the fusion constructs VE-cadherin-FK506 and VE-PTP-FRB were separated by an internal ribosomal entry site (IRES). This cDNA construct was then inserted into the VE-cadherin locus of the target mice which led to the replacement of endogenous VE-cadherin. Mice containing this bi-cistronic construct express the two cDNAs under the endogenous VE-cadherin promotor, but as separate proteins. NADPH oxidase 4 (Nox4) floxed mice were a gift from Dr. Viswanathan Natarajan. Calcium indicator Salsa6f (Jackson cat. #IMSR_JAX:031968) and Piezo1 floxed B6.Cg-Piezo1tm2.1Apat/J (Jackson cat. #IMSR_JAX:029213) mice were purchased from vendor. PMN specific genetic deletion was generated by crossing indicated transgenic mice with Catchup mice. Deletion of specific genes were confirmed by Western blotting.

METHOD DETAILS

Isolation of transmigrated and non-transmigrated PMN

Segregation method of transmigrated and vascular PMNs have been adopted from Paul Frenette (see results section: Adherens junctions (AJs) enhance bactericidal function of transmigrating PMN).[36] PMN were mobilized to lung of 8-10 weeks old male Catchup (heterozygous) or non-labelled C57BL/6-background mice by exposure to 1mg/ml or 5mg/ml (for short duration PMN transmigration kinetics) in nebulized LPS (Sigma, *Escherichia coli* O55:B5) inside the fumigation chamber. 20 μg of α-Ly6G-BV421 antibody (Biolegend, #127628) was i.v. injected 2 minutes before sacrifice. Lungs were perfused with 10 ml of PBS through right ventricle of heart and collected for PMN isolation, biochemical, and histopathological analyses. For PMN isolation, a single cell suspension was prepared by digestion of minced lung lobes with collagenase A (1 mg/ml; Millipore-Sigma # SCR103) at a 37^{0}C shaking water bath for 45 min. Digested lung samples were passed through 16-17G needle and filtered through 40 μm cell strainer (Thermo Fisher, #08-771-1). Red blood cells were removed by using RBC lysis buffer (Thermo Fisher, #00-4333-57). A single cell suspension prepared from Catchup (heterozygous) mice were directly subjected to flow sorting for separation of td-Tomato-positive, or double td-Tomato and α-Ly6G-BV421-positive PMN. Suspension from non-labelled mice were further stained with α-Ly6G-AF594 antibody (Biolegend, #127636) before sorting for α-Ly6G-AF594, or dually labelled α-Ly6G-AF594 and α-Ly6G-BV421-positive cells.

Fluorescence-activated cell sorting (FACS) and flow cytometry

PMN, labelled with td-Tomato (or α-Ly6G-AF-594) and td-Tomato and α-Ly6G-BV-421 (or α-Ly6G-AF-594 and α-Ly6G-BV-421), were sorted in a sterile environment by MoFlo Astrios and MoFlo Astrios EQ (Beckman Coulter) cell sorter equipped with 405, 488, 561 and 635 nm lasers, and collected in RPMI-1640 medium (Thermo Fisher #72400047). Gates were initially established on forward and side scatter, based on granularity and relative size. Aggregates were gated out accordingly. Selective gates were drawn to sort the single positive and dual positive PMN. Software SUMMIT, 6.1 (Beckman Coulter) was used for sorting and analysis. CytoFLEX-S (Beckman) flow cytometer, equipped with 405, 488, 561 and 635 nm lasers, was used for data acquisitions of peripheral blood PMN. Data analyses were performed by Kaluza Analysis 2.1 (Beckman) software. The number of neutrophils in peripheral blood of control Piezo1$^{fl/fl}$ and Piezo1$^{\Delta PMN}$ mice was quantified using flow cytometry. Blood analyzer, Siemens Advia 120, was used for absolute counts of PMN from blood.

As conventional flow cytometry is limited for multicolor analysis, we used spectral flow cytometry (Cytek Aurora, Cytek Biosciences') and spectral unmixing to distinguish the differentially expressed surface markers in transmigrated and non-transmigrated PMNs. Briefly, samples were run through a 5-laser spectral flow cytometer (Aurora, Cytek Biosciences). Appropriate quality control was performed per the manufacturer recommendations. For single stained controls, beads (Invitrogen) were used and were acquired first, followed by samples. Cells were used as controls to determine autofluorescence and to determine live/dead staining. Unmixing matrix with autofluorescence extraction was calculated using SpectroFlo 2.2.1 software (Cytek Biosciences). Unmixed data was then analyzed using Kaluza 2.1 software (Beckman Coulter). Fluorescence minus one (FMO) controls were used to determine appropriate gating. Expression changes were calculated by measuring the Median Fluorescent Intensity (MFI). Gating strategy where cells were gated on scatter properties followed by singlets. Live cells negative for staining with Zombie-NIR live/dead stain were selected for further analyses. Gating strategy using Fluorescence minus one (FMO) controls are shown.

Bacterial culture

E. coli DH5α (ATCC #25922GFP) and *Pseudomonas aeruginosa* (PA-GFP-01 strain; gift from Dr. Terry Manchen, University of California, Berkeley, CA[72]) constitutively expressing GFP, were grown in LB Broth (Sigma L3522) with carbenicillin (Goldbio, #C-103-5). Concentration of *E. coli* at OD 0.4-0.6 was calculate (https://www.agilent.com/store /biocalculators/calcODBacterial.jsp) using Agilent *E. coli* calculator. The titer of *P. aeruginosa* was calculated from colony forming units (c.f.u) obtained from serial dilution of

over-night grown culture plated on LB-carbenicillin plates. Culture, storage, and handling were followed in BSL2 environment according to the University of Illinois at Chicago's Institutional Biosafety Committee.

Phagocytosis and intracellular bacterial killing *in vitro*

PMN mediated bacterial phagocytosis and killing assay was adapted from Gille et al..[74] and Isberg and Falkow[75] In brief, constant number of PMN were incubated with GFP-E. *coli* at 20:1 (cell: bacteria) ratio for 30-90 min for ingestion and non-phagocytosed bacteria were removed from incubation medium by gentle centrifugation at 200-300 rcf. Bacteria killing was assessed 30-210 min later. Internalized bacteria were released from PMN by 1% Triton-X. Percentage of bacterial killing was normalized to the ingestion sample.

Colocalization of Nox4 with phagosomal and phago-lysosomal markers

HL-60 cells were transduced with Nox4-mGFP-tagged lentiviral particles (OriGene, #RC208007L4V) and expressing cells were selected with puromycin. The Nox4-mGFP expressing HL-60 were differentiated as described above, plated on a glass bottom dish coated with fibrinogen, and were allowed to adhere for 1h. *Pseudomonas aeruginosa* at 1:50 (cell: bacteria) ratio were added to the dish on ice to allow for the bacteria to settle down as described elsewhere.[76] The HL-60 derived PMN were then incubated at 37^0C for 5, 20, and 60 min, fixed, and stained with phalloidin and immunofluorescent stained with antibodies for the early phagosome marker RAB5A (Proteintech, #11947-1-AP), the late phagosome marker RAB7 (Cell Signaling, #9367), and the phagolysosomal marker LAMP1 (Cell Signaling, #15665), respectively. Z-stacks images were captured on the Carl Zeiss LSM 710 BiG confocal microscope driven by the ZEN software. ImageJ (Version 1.53r) and the plugin JaCoP[77] were used to analyze he colocalization of Nox4 with the markers. 3D surface rendering of images was applied using the surface module in Imaris (Version 9.5). In brief, the images of Nox4, F-actin, or phagosome and lysosome markers were individually reconstructed with surface segmentation threshold before compositing into a single image.

Manipulation of restrictiveness of endothelial junction *in vivo*

The restrictiveness of endothelial junction in mice was decreased by IV injection of 20 μg functional blocking α-VE-cadherin antibody (α-CD144, clone 11D4.1; BD Biosciences #555289).[41] Isotype matched antibody (IgG2a κ, clone R35-95, BD Biosciences # 559073) was IV injected as control. 1h post administration of antibody, animals were subjected to LPS inhalation (1mg/ml in total volume of 5 ml) and used for the experiments at 3 h post-exposure. Transmigrated and non-transmigrated PMN were isolated as described above. Restrictiveness of EC junction was increased by IV injection of 125 μg (6.2 mg/kg) rapalog everolimus (Sigma SML2282) into $Cdh5^{tm4(Cdh5/Fkbp,Ptprb/Mtor*)Dvst}$ mice[38] at 8 h and 4 h before exposure of nebulized LPS. Vehicle was used as control. PMNs derived from bone marrow or lung were treated with 5 nM of everolimus in control experiments.

Fabrication of microfluidic device

Microfluidic devices were fabricated using soft photolithography.[78] Briefly, a glass photomask with the desired microfluidic channels was designed using AutoCAD and fabricated from company (Fineline-imaging Inc). The microchannels were then transferred from the photomask onto a 3" silicon wafer using dry film protocols.[79] Microchannels were replicated into the Polydimethylsiloxane (PDMS, Sylgard™ 184, Dow Corning, USA) by casting base and curing agent (10:1 wt/wt) on the silicon wafer, which was cured on a hotplate of 80^0C for 2h. PDMS slabs with the microchannels were then bonded onto 1" × 3" glass slides (#12-544-4, Fisher Scientific, USA) using oxygen plasma (PE-50, Plasma Etch Inc, USA). Inlet and outlet holes were punched using a biopsy punch before the bonding. The microchannels include a parallel-array of diamond-shaped with 4-5 μm gap size or circular posts with 5 and 200μm gap size, and the heights of the channels were either 20μm or 50μm, respectively.

Chemotactic PMN transmigration through trans-well pores

PMNs were chemotactically transmigrated through trans-well hanging cell inserts with various pore diameters (polyethylene terephthalate inserts were 3 μm (Millipore MCSP24H48), 5μm (Millipore MCMP24H48), 8 μm (Millipore MCEP24H48) in diameter; polycarbonate inserts were 12 μm (Millipore PIXP01250) in diameter). 1 μM fMLP (N-Formyl-Met-Leu-Phe; Sigma #F3506) chemo-attractant was added to 500 μL of RPMI-1640 medium in 24 well cell culture plate. $5x10^5$ bone marrow PMNs were added on top of hanging cell insert and allowed to chemotactically transmigrate for 90 min. Transmigrated PMNs were collected from both the bottom layer of the insert and the medium. PMN numbers were calculated by automated cell counter (Countess 3, Thermo Fisher).

PMN isolation from bone marrow

Femur and tibia bones were removed from mice immediately after euthanasia by ketamine/ xylazine/ acepromazine. Bones were initially kept in RPMI medium containing heparin (10 U/ml), and then flushed with HBSS-prep buffer (Ca^{2+} and Mg^{2+}–free HBSS with 20 mM HEPES, 0.1% BSA). Cell suspension was filtered through 40 μm cell strainer (Falcon 352340), centrifuged at 300g for 5 min at 4^0C to pellet down. Cells were gently resuspended in 1 ml of HBSS buffer containing Ca^{2+} and Mg^{2+} and overlayed carefully over 5 ml of 63% Precoll (GE Healthcare, #17-0891-01) and centrifuged for 30 min at 500g at 4^0C with medium break. PMNs were collected from the bottom of the gradient, treated with RBC lysis buffer (NH_4Cl 8.03g/L, $KHCO_3$ 1g/L, EDTA-4Na 0.002%) for 1 min on ice. Cells were pelleted at 300g, 5 min, 4^0C, and resuspended with 500-800 μL of RPMI or HBSS. Cell densities were kept less than $10x10^6$ per ml.

Please cite this article in press as: Mukhopadhyay et al., *trans*-Endothelial neutrophil migration activates bactericidal function via Piezo1 mechanosensing, Immunity (2023), https://doi.org/10.1016/j.immuni.2023.11.007

Adoptive transfer

Bone marrow derived PMNs from donor control and Piezo1$^{\Delta PMN}$ mice were transmigrated through microfluidic device, or sheared by rheometer, before transferring *i.t.* to syngeneic recipient mice of the same age. In the experiments with Nox4 inhibitor, bone marrow murine PMN were treated with 10μM GKT137831 or vehicle prior i.t. adoptive transfer of the cells into lungs of mice. Recipient mice were prior infected with 1x10^6 GFP-expressing *Pseudomonas aeruginosa*. After 16 hours, recipient mice were euthanatized at BSL2 facility.

Clearance of lung infection

Mice were infected with 1x10^6 GFP-expressing *Pseudomonas aeruginosa* through intra-tracheal route. 16 h post-challenge, lungs were perfused with HBSS, right lung lobes were excised for plating of bacteria into agar plates whereas left lung was inflated by 10% formaldehyde solution (Sigma HT501128) applied through trachea. 1 mg of left lung fragment was homogenized and plated upon serial dilution. Bacterial colonies formed per mg lung lobe were counted at multiple dilutions.

Immuno-histochemistry

Tissue processing, embedding, and sectioning of murine lung samples were performed by UIC's Research Histology Core. Briefly, following the fixation in 10% formalin, murine lung samples were loaded into ASP 300s automated tissue processor (Leica Biosystems) and dehydrated by a series of ascending graded ethanol, cleared in xylene, and infused with paraffin following a preset protocol. Samples were then embedded in paraffin (Paraplast, Leica Microsystem), and five micrometer sections were cut at three levels with 200μm step. Sections were mounted on positively charged slides, dried, and baked at 60°C for an hour. The lung samples were stained with H&E was by UIC's Research Histology Core and imaged by UIC's Research Tissue Imaging Core. Briefly, adhered sections were deparaffinized, stained with H&E, and dehydrated on Leica Autostainer XL (Leica Biosystems) following a preset protocol. Sections were mounted with Micromount media (Leica Biosystems) on CV5030 automated cover-slipper (Leica Biosystems). Stained slides were scanned at 40X magnification on Aperio AT2 brightfield digital scanner (Leica Microsystems). Leica Aperio Imagescope software was used to analyze the images for determining lung injury index.

Assessment of Acute Lung Injury (ALI) Score

The score was calculated according to previously described method.[80] Briefly, histology of the lung was used to score for: (A) PMNs in the alveolar space, (B) PMNs in the interstitial space, (C) hyaline membranes, (D) proteinaceous debris filling the airspace, and I alveolar septal thickening. Each item (a-e) was given a score between 0-2. The total score of the field was calculated by:

$$ALI = \frac{20A+14B+7C+7D+2E}{F} * 100$$

where A-*E* is the variable described above and *F* is the number fields analyzed. A minimum score of zero would represent a healthy lung and a maximum score of 1 represents a lung with severe acute lung injury.

Immunofluorescent staining

Immunofluorescent staining was performed to study the clearance of *Pseudomonas aeruginosa* in murine lung samples. Briefly, adhered sections of murine lung samples were deparaffinized and re-hydrated with descending graded ethanol. Heat antigen retrieval was then performed with a pH 6.0 sodium citrate buffer. The slides were then stained with α-GFP antibody (Santa Cruz Biotechnology, # sc-9996; 1:50) and α-PECAM1 antibody (Abcam, # ab28364; 1:50), or α-GFP antibody (Santa Cruz Biotechnology, # sc-9996; 1:50), α-PDPN antibody (DSHB, #8.1.1; 1:100), α-MPO antibody (abcam, #ab9535; 1:25) overnight at 4°C. The slides were then incubated with appropriate secondary antibodies. Images of stained samples were captured on the Carl Zeiss LSM 710 BiG confocal microscope driven by the ZEN software. ImageJ (Version 1.53r) was used to quantify the number of GFP-positive bacteria and PMN, the distance between bacteria and PMN, bacterial engulfment events, PMN to bacteria ratio.

Cell culture and lentiviral transgenesis

3 to 5 targeting shRNA containing lentiviral particles were purchased from Sigma. Lentivirus were added to HL-60 cells at a 1: 2 (cell: virus) ratio. Infected cells were selected by 2 μg/ml of puromycin (Sigma P8833). The most efficiently depleted cloned were selected for further analyses.

In vivo lung intravital imaging of transmigrated neutrophils

Surgical methods for gaining access to lung was previously described.[81] Briefly, mice anesthetized mice received intravenous injection via retro-orbital sinus of 10 μg per mouse Alexa594-labeled α-Ly6G antibody to stain total PMN before the induction of LPS injury. Mice inhaled 5mg of aerosolized LPS (Lipopolysaccharides from Escherichia coli O55: B5, L2880, Lot#028M4094V; Sigma-Aldrich) dissolved in PBS using nebulizer connected with inhalation box (Compressor nebulizer, MODEL: NE-C30; OMRON). Lungs were imaged after 4 hours post-LPS. Intravenous injection via retro-orbital sinus of SeTau647(SETA BioMedicals)-labeled α-CD31 antibody (25 μg/mice) (390, Biolegend) and BV421-labeled α-Ly6G (Biolegend) antibody (10 μg/mice) were used to stain intravascular PMNs and lung microvascular structures before surgery. The multi-color images were collected as described for calcium imaging. ImageJ and Origin (OriginLab) and customized LabVIEW programs (National instruments) were used to quantify PMN dynamics.

Lung intravital calcium imaging during PMN transendothelial migration

Lung intravital calcium imaging was performed based on Tsukasaki et al.[82] Briefly, PMN calcium dynamics in mouse lungs was assessed at 24 hours post-endotoxin challenge induced by i.p. LPS. Intravenous injection via retro-orbital sinus of SeTau647(SETA BioMedicals)-labeled CD31 antibody (25 μg/mice) (390, Biolegend) were performed to stain PMNs and lung microvascular structures before surgery. A resonance-scanning two photon microscope (Ultima Multiphoton Microscopes, Bruker) with an Olympus XLUMPlanFL N 20x (NA 1.00) and Immersion oil (Immersol W (2010); Carl Zeiss) were employed to collect multicolor images (Dichroic mirror; 775 long pass filter (775 LP; Bruker), IR blocking filter; 770 short pass filter (770 SP; Bruker), Emission filter; 546/SP nm for GCaMP (FF01-546/SP; Semrock), 595/60 nm for tdTomato (Bruker) and 708/75 nm for SeTau647 (FF01-708/75-25; Semrock) with 940 nm excitation (Laser power: 18.8 mW/cm^2 at back aperture of objective) at video rate. Lung imaging data containing motion artifacts were stabilized by using our own computer vision algorithms.[81,82] (https://github.com/YoshiTsukasaki/CoVSTii or https://uofi.box.com/v/StandaloneCoVSTii.) ImageJ 1.53q and Origin 2022b (OriginLab) and customized LabVIEW programs (National instruments) were used to quantify PMN calcium dynamics. Video S1 demonstrates temporal changes in cytosolic [Ca2+] in PMN before, during, and after transmigration through lung endothelial junction labeled by anti-PECAM1antibody (blue).

Cremaster muscle Intravital calcium imaging during PMN transendothelial migration

PMN transmigration in cremaster muscle was induced by injection of 250 μl of MIP-2 (4 μg/ml; R&D Systems) solution intrascrotally. PMN transmigration in cremaster muscle was 1 h after MIP-2 application. Surgical methods for gaining access to cremaster muscle were previously described.[83,84] An Olympus BX upright microscope with LUMPlanFLN60x/1.00W objective and Hamamatsu ORCA Flash 4.0 high-speed cameras (VIVO intravital imaging system, 3i) was used to collect bright field and dual-color images. The images of GCaMPf and tdTomato were collected using EGFP (FITC/Cy2) and DSRed (TRITC/Cy3) (Chrome) filter sets. Respectively. Videos, added as Video S4, were acquired, processed, and analyzed by using SlideBook (3i) and imageJ and was captured at rate, 2 seconds/frame.

Imaging calcium in PMNs migrating through microfluidic pores

HL-60-derived PMN stably expressing control and Piezo1 shRNA were used in this study. Prior to microfluidic transmigration PMNs were diluted in HBSS buffer (with Ca^{2+} and Mg^{2+}; Thermo Fisher, # 14025092) to 10^4 – 5x10^4 cells per ml. Cells were stained with Fluor-4 AM dye (1 μg/ml; Invitrogen, #F14201) and cell mask membrane stain (Thermo Fisher, #C10046) in suspension for 5 min. After staining, 1ml of cell suspension was loaded into a 5 ml syringe (NORM-JECT ®, Air-Tite Products Co., Inc) and connected with microfluidic device by tubing. Cells were pumped (KD Scientific Inc, # Legato 180) into the device at a minimum volumetric flow rate of 20μl/min flow rate to squeeze through the gaps between the posts. Fluo4 and cell mask membrane stain were imaged using FITC (480/40Ex; 535/50Em) and mCherry (560/40Ex; 590lpEm) filters and LED light source (Xylist120). Time-laps images were captured using an Olympus IX-83 epi-fluorescence microscope equipped with a high-resolution sCMOS camera (Zyla 5.5, Andor Inc). Images were captured at 0.5fps for both channels. Cellsens software was used to record and analyze the data.

Computational modeling and 3D simulation

We coupled the finite element method (FEM) for the cell membrane with a boundary element method of Stokes flow[85] to simulate a PMN-like cell passing through a circular pore at the inter-endothelial gap. The PMN was modeled as an isotropic hyperelastic spherical shell with a typical diameter of 8.5 μm. The initial tension of the cortical cytoskeleton was set to 35 pN/μm.[86] The cortical tension under deformation was modeled as:

$$\sigma = \sigma_0\left(1 + \frac{1}{J_{max} - J} - \frac{1}{J}\right) \quad \text{(Equation 1)}$$

where $J = A/A_0$ is the area change ratio and A and A_0 are current and initial area.$J_{max} = 2$ is the maximum allowed area change.[86] $\sigma_0 = 35\ pN/\mu m$ is the initial cortical tension. In Equation 1, the tension will reach infinity when area change approaches 2.0, while it gives infinitely large compression stress to prevent collapse when J approaches 0.0. When J=1 (no area deformation), it gives the initial tension σ_0. The interior of the PMN is filled with an incompressible viscous fluid. Its dynamics is solved using the boundary element approach[85] with a viscosity of 400 Pa, which is 5 orders higher than the viscosity of water (0.001 Pa s).[87] The detailed coupling algorithm was previously published.[85] The contribution of the nucleus in resistance force was ignored due to its "three-lobed" structure, which has a high surface-area-to-volume ratio, leading to negligible resistance. Endothelial cells, which form the circular pore, are modeled as 1-μm thick rigid plate of smoothly rounded edge with radius of 0.5 μm. The diameter of the pore is varied from 0.5 μm to 5 μm based on experimental measurements of the inter-endothelial gap.[13]

We used COMSOL Multiphysics to simulate the flow field in the microfluidic device under given flow rate. The device geometry was imported from a CAD model. The finite element method was used to predict the velocity, pressure, and shear stress in the channel. The shear stress is calculated by multiplying the shear rate by the water viscosity (0.0012 Pa s). Realtime details of computational 3D modeling of membrane tension in a PMN passing through an endothelial junctional pore is shown as Video S2. The color map shows PMN membrane tension and pressure experienced by the plasma membrane. The simulation on provided Video S2 are based on the pore of 2 μm in diameter and PMN diameter of 8.5 μm.

Please cite this article in press as: Mukhopadhyay et al., *trans*-Endothelial neutrophil migration activates bactericidal function via Piezo1 mechanosensing, Immunity (2023), https://doi.org/10.1016/j.immuni.2023.11.007

Calculating activation probability of Piezo1 channel

Correlation between critical force on membrane to the deformability and activation of Piezo1 channel was obtained from Lin et al.[47], Lewis and Grandl,[88] Cox et al., [89] and Yang et al.[90] Mechanical spring constant values of Piezo1 was used from studies by Lin et al.[47] The critical force on membrane was estimated as 18 pN to activate Piezo1 and the critical tension (half-activation tension) as 0.6 kBT nm^{-2}, which is between the values of 0.35 kBT nm^{-2}[88] and 1.2 kBT nm^{-2}.[89] These values can be translated to 1440 pN/μm, 2468 pN/μm, and 7820pN/μm, respectively. Recently, Yang et al.[90] calculated a half maximal activation tension of about 1900 p/μm, based on the measured in-plane membrane area expansion and stiffness constant of Piezo1. Lewis and Grandl measured Piezo1 currents evoked by membrane stretch in three patch configurations by experiments.[88] The current curve is fitted as $I = I_{max}/(1+\exp(-(T- T_{50})/k))$ where I is current, I_{max} is the plateau, T is tension, T_{50} is the tension of half-maximal activation, and k is the slope factor. For +5 mmHg pre-pulse, values were obtained as $I_{max} = 0.85\pm0.01$, $T_{50} = 1.4\pm0.1$ mN/m, $k = 0.7\pm0.1$ mN/m. We consider the activation probability of PIEZO1 under tension T as:

$$P(T) = \frac{I}{I_{max}} = \frac{1}{1+e^{-\frac{T-T_{50}}{k}}} \quad \text{(Equation 2)}$$

When T is large, the probability P approaches 1. When $T= T_{50}$, P(T)=0.5. When T=0, $P(0)=1/(1+\exp(T_{50}/k))=0.119$. Using this formula, we determined the activation probability of PIEZO1 in our simulations and plotted the right Y axis based on the membrane tension T, obtained from simulations. Similarly, we also predicted the activation probability of PIEZO1 based on the pressure on the membrane by

$$P(p) = \frac{1}{1+e^{-\frac{p-p_{50}}{k}}} \quad \text{(Equation 3)}$$

Where p is the pressure on the membrane, and $p_{50} = 659$ Pa and k=329.5 Pa. $p_{50} = 659$ Pa is estimated by $T_{50} = 1.4\pm0.1$ mN/m and PMN diameter (8.5μm) based on the Young-Laplace equation.

For computational modeling of the transmigration process, we used our in-house code (Lu and Peng, Physics of Fluids, 31:031902, 2019), in which finite element modeling of cell membrane is coupled with the boundary integral method analysis of surrounding fluid. It is written in Fortran. We also used open-source code Paraview 5.7.0 for visualization.

Mouse survival experiments

PMN-specific Piezo1$^{-/-}$ and NOX4$^{-/-}$and their respective floxed mice were infected with GFP-expressing *Pseudomonas aeruginosa* (PA-GFP-01 strain) at 1x10^6 concentration by intra tracheal route at the BSL-2 facility. 9 animals per group were used for the survival studies.

RNA isolation

Total RNA from flow sorted lung PMNs were isolated by RNeasy Plus kit (Qiagen, #74034). PMNs sorted from 6 mice were pooled into 1 sample. Sorting was performed at different days to prepare three independent sample sets. Concentrations of isolated RNA samples were measured using Nanodrop 1000 (Thermo Fisher) at 260 nm, and purity was assessed by 260/ 280 nm optical density ratio. RNA samples were transcribed to complementary DNAs with random primers using ''high-capacity cDNA reverse transcription kit'' (Thermo Fischer, #4368814).

RT-qPCR

Quantitative gene expressions were determined by real-time PCR upon mixing the cDNAs with FastStart Universal SYBR Green Master (Rox: Millipore Sigma, #4913914001) with specific qPCR primers. Amplification of PCR reactions were carried out on ABI Prism 7000 system and real-time amplification data was analyzed on Quant studio7 Flex Real-Time PCR System (Thermo Fisher). Results were calculated using the comparative CT-method,[91] and expressed relative to the expression of the housekeeping gene.

RNA sequencing

RNA quality and quantity was assessed using the Agilent bio-analyzer. All samples showed RNA integrity number > 8. Strand-specific RNA-SEQ libraries were prepared using a TruSEQ mRNA RNA-SEQ library protocol (Illumina provided). Library quality and quantity was assessed using the Agilent bio-analyzer and libraries were sequenced using an Illumina NovaSEQ6000 (Illumina provided reagents and protocols).

RNAseq analysis of transmigrated and non-transmigrated neutrophils

Gene expression quantification

Raw reads were trimmed to remove Truseq adapters and bases from the 3' end with quality scores less than 20 using cutadapt (Martin, 2011); trimmed reads shorter than 40bp were discarded. Trimmed reads were aligned reference genome mm10 using STAR aligner.[92] ENSEMBL gene expression was quantified using FeatureCounts.[93]

Please cite this article in press as: Mukhopadhyay et al., *trans*-Endothelial neutrophil migration activates bactericidal function via Piezo1 mechanosensing, Immunity (2023), https://doi.org/10.1016/j.immuni.2023.11.007

Differential expression

Differential expression statistics (fold-change and p-value) were computed using edgeR,[94,95] using generalized linear models to correct for batch effect while testing for differences between LPS treatment groups. P-values were adjusted for multiple testing using the false discovery rate (FDR) correction of Benjamini and Hochberg.[96] Significant genes were determined based on an FDR threshold of 5% (0.05).

Pathway analysis

We ran the core analysis in Ingenuity Pathway Analysis on differentially expressed genes to obtain canonical pathways and upstream regulators that were associated with differentially expressed genes. Significantly enriched pathways were determined based on FDR-adjusted p-value < 0.05. Groups of significantly enriched pathways with similar function were grouped into super-pathways based on manual curation of the terms. Z-scored log-scaled normalized gene expression levels for all differentially expressed genes within these super-pathways were plotted in heatmaps.

Intracellular ratiometric Ca^{2+} measurements

Dual-color images were captured simultaneously for tdTomato and Fluo-4. Ratiometric calcium signal analysis was performed according to previously published method.[97] For comparisons of relative changes in $[Ca^{2+}]_{cyt}$ a cross-sectional view of the intensity values of Fluo-4 normalized to tdTomato intensity values was generated at each time point using Image J, and the relative changes in $[Ca^{2+}]_{cyt}$ were calculated.

Western blotting

PMNs were lysed using RIPA buffer (Sigma-Aldrich Cat. R0278) and concentration was determined using Bicinchoninic acid assay/Pierce BCA Protein Assay Kit (Thermo Scientific, REF. 23225). Samples were resolved by SDS-PAGE, transferred to 0.45um Nitrocellulose Membrane (Bio-Rad Cat. #1620115) and incubated overnight with Piezo1 (Protein Tech, 15939-1-AP), NOX4 (Novus, NB110-58849), Vinculin (Abcam, ab129002) antibodies. After incubation with secondary antibody, protein was detected by chemiluminescence using PICO PLUS (Thermo scientific, REF 34580) and captured using Autoradiography films (LabForce, 1141J51).

ROS generation assay

Generation of reactive oxygen species by HL-60-derived PMN stably expressing control, Piezo-1 and NOX4 shRNA were measured by amplex red reagent (Invitrogen A22188). Amplex red (10-acetyl-3,7-dihydroxy-phenoxazine) detects H_2O_2 (a direct product of Nox4 activity, or by-product of free oxygen radicals) upon converting to resorufin (Ex_m: 571nm; Em_m: 585nm; absorbance: 560nm). Phorbol-ester was used to enhance the signal.

NETosis assay

FACS-sorted transmigrated and non-transmigrated neutrophils were incubated with GFP *Pseudomonas aeruginosa* @ 1: 10 m.o.i. for 1h. $1x10^5$ neutrophils were used per assay. Post incubation supernatant was used for elastase ELISA following manufacturers (mouse neutrophil elastase ELISA kit; ab252356) protocol. Frequency of NET formation is plotted as OD at 450 nm.

Neutrophil longevity assay

Transmigrated and non-transmigrated neutrophils sorted by FACS were cultured *ex vivo* in RPMI supplemented with a supernatant of mouse primary lung microvascular endothelial cell (7:3). Viability of neutrophils were tested at different time points by staining with trypan blue.

QUANTIFICATION, STATISTICAL ANALYSIS AND REPRODUCIBILITY OF EXPERIMENTS

Ratiometric calcium signal quantitation was plotted by Origin Pro, rest of the graphs were generated using GraphPad Prism. All data were expressed as mean ± standard error. One-way Anova was used for pairwise comparison with multiple groups, and two-tailed *t*-test was used to determine statistical significance. Number of samples or mice per group, replication in independent experiments and statistical tests are mentioned in the figure legends. For studies in mice, significance level of 0.05 and power of 0.9 were used to estimate the group sizes (JMP release 6 software: SAS, Cary NC). In RNA-seq analyses, the $\log_2$ fold-change was used to determine the effect size.